EXPERIMENTAL DEFORMATION OF POTASSIUM FELDSPAR SINGLE CRYSTALS

A Thesis by

CLAIRE P. MARTIN

Submitted to the Office of Graduate and Professional Studies of
Texas A&M University
in partial fulfillment of the requirements for the degree of

MASTER OF SCIENCE

Chair of Committee,	Andreas K. Kronenberg
Committee Members,	Judith S. Chester
	Will Lamb
	Miladin Radovic
Head of Department,	Julie Newman

May 2021

Major Subject: Geology

ABSTRACT

Several naturally occurring potassium feldspar single crystals have been shortened in triaxial deformation experiments in the [012] direction to activate both (010)[001] and (001)1/2[110] slip systems. Sanidine single crystals have been shortened in the [001] direction to activate the (121)[101] slip system. Experiments were conducted in a Griggs solid-medium apparatus at temperatures of 650-950°C, strain rates of $\dot{\varepsilon}$=1.6*10^{-6}s^{-1} to 2.1*10^{-4}s^{-1} and at a confining pressure of 1500 MPa. Samples chosen have various Al/Si ordering, crystal symmetry, water content and hydrogen speciation. At lower temperatures (T≤700°C and $\dot{\varepsilon}$ = 10^{-6}s^{-1}), feldspars oriented for slip exhibit differential yield stresses of 204-613 MPa. Many exhibit peak stresses (718-556 MPa) followed by strain softening. One sample reached a nearly constant stress and another showed strain hardening. At higher temperatures (T≥900°C), samples exhibit yield stresses of 132-227 MPa before approaching constant flow stresses (PF-2, AF-2) or hardening (PF-7, SF-2, BF-2). Differential stresses decrease with increasing temperature and show a positive correlation with strain rate. The strain rate and temperature dependencies of feldspar strength can be described equally well by a thermally activated power law, exponential glide law, and Peierls lattice resistance law with a common temperature dependence given by activation enthalpy (H*) = 281.7 kJ/mol. Best fit values of the power law, exponential law and Peierls law are n=7.70, α=0.0315 MPa^{-1}, and σ_p=44.4 MPa, respectively. The excellent fit of these creep laws suggest that dislocation slip is predominant but other mechanisms are active as well. All samples show undulatory extinction due to dislocation slip and all reach the critical resolved stress required for mechanical twinning. Sample-scale cleavage fractures and microcracks are also present in deformed samples with some microstructures that suggest simultaneous brittle-plastic deformation. The combined mechanical and microstructural results reflect brittle-plastic deformation of feldspars, similar to the feldspar microstructures found in naturally deformed

rocks of the middle to lower continental crust. The mechanical results for these potassium feldspars are remarkably similar given the differences in ordering, symmetry and water content of the samples.

CONTRIBUTORS AND FUNDING SOURCES

Contributors

This work was supervised by a thesis committee consisting of Professor Dr. Andreas Kronenberg, Professor Dr. Judith Chester, and Professor Dr. Will Lamb of the Department of Geology and Geophysics and Professor Dr. Miladin Radovic of the Department of Material Science.

The experiments and analyses were conducted in part by Abhishek Prakash of the Department of Geology and Geophysics and are being prepared for publication.

All other work for the thesis was completed by the student independently.

Funding Sources

Graduate study was supported by a teaching fellowship from Texas A&M University and a research fellowship from Dr. Andreas Kronenberg.

NOMENCLATURE

T	Temperature
Pc	Confining Pressure
Pp	Pore Pressure
$\dot{\varepsilon}$	Strain Rate
SEM	Scanning Electron Microscope
EBSD	Electron Backscatter Diffraction
IR	Infrared Spectroscopy
XPL	Cross polarized light
PPL	Plain polarized light
PBC	Periodic Bond Chain

TABLE OF CONTENTS

Page

LIST OF FIGURES

Page

LIST OF TABLES

Page

1. INTRODUCTION

The objectives of this experimental deformation study are to investigate the mechanical properties, predominant deformation mechanisms and microstructures of a range of potassium feldspar single crystals at experimental conditions that might favor the same types of deformation at conditions of the middle to lower continental crust. The crystal chemistry and structure of feldspars are complex, with deformation and recovery processes that may depend on variations in composition, crystal symmetry, Al-Si ordering, internal twinning and exsolution microstructures. To simplify the complexity of feldspar deformation, I chose to deform single crystals of a simple end member composition single crystals in the crystallographic [012] and [001] directions, following the original single crystal deformation experiments of Willaime et al. (1979). Feldspar single crystals shortened in the [012] direction at elevated pressure and temperature activate two prominent slip systems the (010) [001] and the (001) 1/2 [110]. The sanidine single crystals shortened in the [001] direction at similar pressure and temperature conditions was done to activate the (121)[101] slip system. This study also follows from the approach taken by Kekulawala et al. (1978) in their study of water weakening in different quartz varieties, combining IR spectroscopy with deformation experiments to identify those hydrous defects that reduce plastic flow strengths. The completion of the thorough IR spectroscopic study I planned for the potassium feldspars of this study was cut short by the failure of the FTIR instrument in the Department of Geology and Geophysics and the extended closure of the IR spectroscopy lab at the Johnson Space Center (Jacobs Research, Houston, TX) due to COVID-19 safety regulations. Preliminary IR spectra were generously provided by Dr. Caleb Holyoke, University of Akron, but I plan to revisit the IR spectroscopic analysis of the feldspar crystals investigated here before and after deformation to obtain quantitative measurements of OH absorption bands and evaluate their hydrogen speciation

and water concentrations. The results of this thesis, supported by these IR measurements will constitute the basis for a journal publication.

The continental crust is largely felsic, with up to 90% of its crystalline rocks made up of quartz and feldspars (Carlson et al., 2008; Fletcher, 2010). The mechanical properties of granite and quartzo-feldspathic rocks at depth are governed to first order by dislocation creep of constituent grains of quartz (Hirth and Tullis, 1992) at temperatures T>300°C (Sibson et al., 1977), with plastic deformation of feldspars becoming important once temperatures reach T>450°C (Sibson et al., 1977; Hirth and Tullis, 1992; Scholtz et al., 1989). However, feldspars make up ~2/3 of the continental crust and predominant lithologies of the lower crust lack any quartz at all (Rudnick and Fountain, 1995; Carlson et al., 2008; Hacker et al., 2015).

Observations of granite deformed in laboratory experiments at temperatures up to 800ºC (Tullis et al., 1977) and natural granitic shear zones deformed at greenschist conditions reveal extensive plastic strains of quartz, while plastic strains in feldspars are limited and changes in feldspar grain shape are largely due to fracture, and frictional displacement on en echelon fractures (Kerrich et al., 1980). At higher experimental temperatures, feldspars of granitic rocks begin to deform plastically (Dell Angelo and Tullis, 1996), and natural amphibolite-grade shear zones with feldspar-dominant and gabbroic lithologies reveal evidence of dislocation glide and creep, accommodated by internal recovery and recrystallization (Miranda et al., 2016). Tectonic models of continental lithosphere deformed at plate margins, are commonly based on the mechanical properties of quartz, representing the friction and flow of crustal rocks, and those of olivine representing the flow of ultramafic rocks of the upper mantle (Buck, 1991; Kusznir and Park, 1987). However, the middle to lower continental crust is known to contain only minor amounts of

quartz, and the reliance of tectonic models on quartz flow laws throughout the crust continues only because the rheology of feldspars is poorly understood (Kohlstedt et al., 1995). My experimental study of potassium feldspar deformation addresses this oversimplification by quantifying the plasticity for one compositional end-member of the feldspars. Based on the importance of water and hydrous defects to the plasticity and creep of quartz by interrupting its fully connected silica tetrahedral, feldspars are also assumed to show water weakening, as hydrous defects and water disrupt these framework silicates. Ultimately, rheologies developed for feldspars may be applied to lithosphere models of plate interiors where basin formation and isostatic adjustments are important (Houseman and England, 1986; Zhong, 1997).

1.1. Rheology of the continental lithosphere

The concept of plate tectonics describes the upper Earth as a small number of thin cold plates (of the lithosphere) that are rigid and undergo little permanent deformation internally, overlying a hot asthenosphere that convects by solid-state flow (Le Pichon et al., 1973). Tectonic displacements, earthquakes and volcanism occur predominantly at plate boundaries (e.g., Bird and Dewey, 1970) and deformation at these boundaries depends on the rheology of the plates at their margins (Freed et al., 2006). Plate rheology depends upon the compositions of rocks of the lithosphere and how the strengths of these rocks depend on pressure and temperature conditions.

Feldspars are ubiquitous in the crust of both continental and oceanic plates; yet their mechanical properties have not received as much attention as those of quartz, owing to their complex crystal chemistry, structure and symmetry, variations in Al-Si ordering, twinning, and internal microstructures. Determinations of lithosphere strength require that we evaluate the rheologies of

this important group of minerals as a function of pressure-temperature-strain rate conditions (Janecke and Evans, 1988), as well as their dependence on water and other volatiles.

The mechanical properties of feldspars are also important to evaluations of the transitional brittle-plastic deformation of granitic fault zones. Granites deformed at mid-crustal levels commonly exhibit evidence of crystal plasticity and creep of quartz while feldspars fail by fracture at the same conditions. Feldspars are observed to deform by multiple simultaneous mechanisms, including plasticity and dislocation glide, fracture, and diffusion creep, depending on their depth and conditions of the continental crust. Water influences the deformation and recovery processes of feldspars, much as it affects the plasticity and creep of quartz. In addition, feldspars may react with interstitial fluids, to form layer silicates and quartz, and thereby weaken shear zones within granitic bodies as strong feldspars are replaced by weak micas (Evans, 1988; O'Hara, 1988; Hippert, 1998).

Mechanical properties of feldspars are thought to influence the qualitative character of continental lithosphere (Figure 1). Yield envelopes for lithosphere constructed at a constant strain rate (Sibson et al., 1977; Brace and Kohlstedt, 1980; Scholz, 1988) depend on friction laws at relatively shallow depths of the upper lithosphere (Byerlee, 1978; Dietrich, 1978), with the mechanics of faulting limited to the upper lithosphere by the intersection of the friction law and flow laws for quartz that govern plastic deformation and creep deeper in the continental crust (Sibson, 1983). Frictional strengths of the lithosphere increase with depth as normal stresses on faults increase, while creep strengths of quartz decrease with depth in the crust, as temperature increases. Quartz flow laws predict very low lithospheric strengths towards the base of the continental lithosphere and significant strength is only realized below the Mohorovicic (Moho) discontinuity where uppermost mantle rock strengths are governed by the deformation of olivine. However, creep in lithologies of

the lower crust are expected to depend on feldspar deformation, with flow laws that likely depend on the presence of water and water weakening processes, similar to those that have been studied for quartz (Bürgmann and Dresen, 2008). While maximum strengths in quartz-rich continental rocks are reached as frictional sliding is replaced at depth by dislocation creep of quartz (at ~300^{o}C), maximum strengths of feldspar-dominated crustal rocks are thought to occur at greater depths (at ~450^{o}C). Depending on the extent of water weakening of crustal and mantle silicates, the mechanical response of continental lithosphere to tectonic stresses has been characterized as: 1) two strong layers with an intervening crustal asthenosphere (the "jelly sandwich" of Turcotte et al., 1984) governed by creep laws for wet framework silicates, quartz and feldspars, and mechanical properties of a dry upper mantle, 2) a consistently strong crustal lithosphere (the "crème-brûlée" of Burov and Watts, 2006) governed by friction in the upper crust and creep laws of dry feldspar in the lower crust, overlying a weak mantle asthenosphere, or 3) a consistently weak lithosphere at plate boundaries (the "banana split" model of Bürgmann and Dresen, 2008) governed by low frictional strengths due to high pore fluids and flow laws of framework silicates, quartz and feldspars, weakened by water and hydrous crystalline point defects (Figure 1).

Widely varying mechanical responses of continental lithosphere to tectonic driving forces depend on variations in composition of the crust, flow laws of the major framework silicates, quartz and feldspars, and their dependence on the presence of water. This experimental study provides new mechanical data and microstructural observations of potassium feldspar single crystals deformed by dislocation glide and accompanying mechanisms as it undergoes brittle-plastic deformation.

1.2. Dislocation Creep of Feldspars and Water Weakening

The deformation of feldspars at high temperatures has been investigated in a number of experimental studies (Table 1; Borg and Heard, 1970; Willaime and Gandais, 1977; Willaime et al., 1979; Kovacs and Gandais, 1980; Tullis and Yund, 1980, 1985, 1987, 1991; Scandale et al., 1983; Wang et al., 1996; Dimanov et al., 1999; Rybacki and Dresen, 2000; Stünitz et al., 2003; Rybacki et al., 2010), generating microstructures that resemble those of feldspars deformed in mid- to lower-crustal shear zones (White, 1975; Vidal et al., 1980; Olsen and Kohlstedt, 1984; Lonka et al., 1998; Kruse and Stünitz, 1999; Kruse et al., 2001; Rosenberg and Stünitz, 2003; Ishii et al., 2007; Bhattacharyya and Mitra, 2011; Franek et al., 2011; Pearce et al., 2011; Brander et al., 2012; Getsinger et al., 2013; Mukai et al., 2014). Coarse-grained polycrystalline feldspars and feldspar-bearing granitic rocks deform by dislocation glide and climb, accompanied by dynamic recrystallization at higher pressures and crack growth, frictional sliding, and cataclastic flow at lower pressures (Tullis and Yund, 1980, 1987; Dell Angelo and Tullis, 1996), while fine-grained feldspars deform by processes of grain boundary diffusion and sliding (Tullis and Yund, 1991; Dimanov et al., 1999; Rybacki and Dresen, 2000; Rybacki et al., 2010).

Much as observed in water-weakening experiments for wet and dry quartzites, polycrystalline feldspars deformed in the presence of water are weaker than dry, but otherwise equivalent, feldspar samples (Figure 2). Direct measurements of water content within silicate grain interiors of polycrystalline samples are difficult and IR spectroscopy of experimentally deformed feldspars to measure OH absorption bands has been attempted in only two studies of feldspar creep (Dimanov et al., 1999; Rybacki and Dresen, 2000). Understanding of water weakening in quartz has benefitted from studies of single crystals (e.g., Griggs and Blacic, 1965; Kekulawala et al., 1978, 1981; Linker 1984; Stünitz et al., 2017) that supplement polycrystalline quartz

deformation results. Individual slip systems of quartz have been studied by deforming single crystals in specific orientations, and their dependencies on different forms of hydrous defects and internal water content have been determined by measuring OH absorption bands in IR spectra. Feldspar single crystals have been deformed in laboratory experiments to investigate their deformation mechanisms, including the slip systems of potassium feldspar and plagioclases of varying composition (Borg and Heard, 1970; Marshall and McLaren, 1977; Willaime and Gandais, 1977; Willaime et al., 1979; Kovacs and Gandais, 1980; Scandale et al., 1983; Stünitz et al., 2003). However, IR absorption spectra were not measured for any of the feldspars single crystals deformed in these studies, and we do not know their water contents or hydrous defect speciation.

Feldspars are fully linked framework silicates that may be weakened by hydrous defects by similar processes that are responsible for water weakening of quartz. Water weakening of silicates was first discovered for quartz (Griggs and Blacic, 1965) and a mechanism by which plastic strengths of silicates might be reduced was first outlined by Griggs (1967), now known as the Griggs-Blacic-Frank mechanism. In this landmark paper, Griggs (1967) proposed a hydrolysis reaction at advancing dislocations, replacing strong Si-O bonds of quartz by hydrogen-bonded Si-OH groups, and went on to propose that hydrolysis reactions might be important to the plastic strengths and creep of all silicates. Experimental studies of silicate deformation have since shown that water reduces creep strengths of olivine (e.g., Chopra and Paterson, 1984; Tielke et al., 2019), pyroxene (Chen et al., 2006), and feldspar (e.g., Tullis and Yund, 1980). However, mechanisms by which water reduces flow strengths differs for orthosilicates, chain silicates, and framework silicates. Olivine, for example, is made up of isolated SiO_4 tetrahedra, bonded by weaker Mg-O and Fe-O bonds, and the climb of dislocations during dislocation creep is facilitated by changes in point

defect population at high water fugacities rather than silicate hydrolysis (Mei and Kohlstedt, 2000). Of all silicates that show water weakening, the mechanism(s) by which feldspar flow strengths depend on water and hydrous defects might be most similar to those of quartz.

Water and hydrous species can occupy surfaces, grain boundaries, dislocations and structural sites of quartz, and much of the water within quartz crystals occurs as fluid inclusions and unfreezable water clusters (e.g., Kronenberg, 1994). During deformation, dislocations can nucleate at molecular water clusters and fluid inclusions (Kirby and McCormick, 1979; McLaren et al., 1983) and dislocation glide and climb may be facilitated by pipe diffusion of hydrous defects to mobile dislocation kinks and jogs. Studies of water weakening of quartz have benefitted from IR spectroscopy, with reductions in strength that correspond to the presence of a broad unfreezable OH absorption band (Figure 3) assigned to molecular water (Kekulawala et al., 1978; Aines et al., 1984). Dry natural varieties of quartz are strong and IR spectra show only small sharp OH absorption bands due to hydrogen defects, while wet synthetic and natural varieties of milky quartz and amethyst deformed at the same conditions are weak and exhibit large, broad OH absorption bands.

Infrared absorption studies have revealed a number of different types of hydrous defects within feldspar interiors (Beran, 1986; Kronenberg et al., 1996; Johnson and Rossman, 2003; Mosenfelder et al., 2015), including OH and H2O on crystallographic structural sites and within fluid inclusions, with concentrations that can exceed those of water contents of coexisting quartz (Kronenberg et al., 1990; Seaman et al., 2013; van der Werf et al., 2017). However, I am not aware of any studies that have combined the experimental deformation of feldspar single crystals with IR spectroscopy to determine what types of hydrous species facilitate dislocation mobility

or to measure internal water contents and thereby quantify water weakening. This experimental study benefits from preliminary IR spectroscopy data collected at the University of Akron but I plan to measure OH absorption bands by IR spectroscopy once I can access the IR laboratory of Dr. Anne Peslier (Jacobs Research, Johnson Space Center, (Houston)) which is currently closed due to the global COVID pandemic.

Previous IR studies of OH absorptions of adularia and ordered triclinic microcline (Figure 4) have shown that their hydrous defects are similar, with principle absorption bands at wavenumbers 3630 cm^{-1} and 3455 cm^{-1} for O-H stretching modes and overtone absorption bands at 5250 cm^{-1} and 5130 cm^{-1} due to combined H-OH bend and O-H stretching modes (Kronenberg et al., 1996). IR and near-IR bands are polarized, with maximum OH absorbances measured in the principal optical α direction and smaller absorbances measured in β and γ vibration directions. Based on these results, OH bands of these feldspars have been assigned to H_2O molecules residing on structural K^+ sites. IR studies of disordered sanidine, on the other hand show polarized OH absorption at 3400 cm^{-1} corresponds to structural OH groups replacing K^+ sites (Libowitzky and Beran, 2004).

In studies of wet quartz varieties, Kekulawala et al. (1978) observed significant increases in strength when crystals were heat-treated prior to deformation, owing to the precipitation of coarse, widely spaced fluid inclusions and loss of fine, dispersed water clusters, even though total water contents were not changed. I plan to measure IR spectra of deformed feldspar samples and compare them with their starting IR spectra to quantify changes before and after deformation.

2. METHODS

The mechanical properties and deformation microstructures of potassium feldspar were determined for triaxially shortened single crystals of varying order, hydrogen and water defects in the [012] and [001] directions at temperatures of 650° to 950°C, strain rates $\dot{\varepsilon}$ of 10^{-6} s^{-1} to 10^{-4} s^{-1}, and the same confining pressure of P_c =1500 MPa. The deformation mechanisms have been evaluated by examining deformed samples using optical microscopy in plane polarized (PPL) and cross-polarized light (XPL), and scanning electron microscopy (SEM) using electron backscatter diffraction (EBSD) to determine crystallographic orientations. My ability to characterize the hydrogen and water defects of feldspar crystals in this thesis must rely on preliminary infrared spectra until I am able to measure OH absorption bands using polarized IR radiation in the principal vibrational directions of potassium feldspar.

2.1 Starting Materials

Crystallographically oriented right-cylindrical specimens (5 mm diam x 10 mm length) were cored for triaxial deformation experiments from several varieties of compositional end-member potassium feldspar crystals ($KAlSi_3O_8$) with varying crystal symmetries, states of Al-Si ordering, and OH contents (Figure 5). The highest symmetry (monoclinic C2/m) feldspars selected for study include clear yellow, microstructure-free disordered sanidine crystals from Madagascar and Pakistan and a clear, light green potassium feldspar from Norway with a baveno growth habit (Figure 5). A clear, twinned adularia crystal from the Swiss Alps has been chosen to represent a transitional monoclinic-triclinic feldspar that retains macroscopic C2/m symmetry while local crystal symmetry varies within micro-domains of triclinic symmetry (Figure 5). The lowest symmetry feldspars (C1) chosen for study include a turbid white, highly ordered microcline of unknown origin and a pink, coarsely perthitic microcline from the Petrick Quarry

of Buchanan Dam, TX (Figure 5). Crystal orientations have been determined based on well-developed crystal faces of the sanidine, baveno, and adularia crystals, cleavage cracks within baveno, adularia, and microcline crystals, and electron backscattered diffraction (EBSD) indexing of polished crystal surfaces of all samples. Crystals were rotated and mounted to core cylindrical samples along the [012] and [001] crystallographic directions. Each core was cut perpendicular to its axis and sample ends ground parallel to each other (to within 0.03 mm) usinga 400 grit SiC powder slurry.

All starting materials were chosen to represent the end-member potassium feldspar composition, although the perthite has distinct albite lamellae within the near-end member microcline (Figure 6). The white microcline contains albite inclusions as well but in smaller volume proportions. The white microcline sample also contains small muscovite and quartz inclusions, resulting from early stages of retrograde alteration during cooling (Figure 6). Electron microprobe analyses obtained at Texas A&M's Materials Characterization Facility (MCF) by wavelength dispersive spectroscopy (WDS) were used to evaluate each sample's bulk and trace element chemistries (Table 2). Polished surfaces for preliminary EDS, quantitative WDS, and EBSD measurements were prepared using a series of Al_2O_3 powder slurries with decreasing grit sizes to 0.3 μm, followed by chemo-mechanical polishing on a Buehler VibroMet vibratory polisher with MasterMet colloidal silica polishing solution. Crystal orientations were determined using EBSD with the FEI Quanta 600 scanning electron microscope (SEM) located at the Texas A&M Microscopy and Imaging Center (MIC). EBSD analyses of feldspar required the use of the SEM in low-vacuum mode at 20 Pa, working distance of ~15mm, accelerating voltage of 25 kV, spot size of 4, copper tape, and no carbon coating (Miranda et al., 2016). EBSD results are plotted as upper-hemisphere pole figures using HKL Channel 5 Mambo Software. Individual

samples were rotated and mounted to precisely cut wooden blocks before embedding in epoxy to core along the [012] and [001] directions. Rotations were determined using a stereonet and verified using WinWulff equal-angle stereonet software.

Before precise sample orientations were determined, doubly polished plates were prepared for Infrared (IR) spectroscopy to estimate water content in order to inform sample characterization as a 'wet' or 'dry' feldspar. Preliminary IR measurements of OH absorption bands were made between wavenumbers of 4000 and 2000 cm-1 by Dr. Caleb Holyoke at the University of Akron using polarized IR radiation and maximum and minimum OH absorbances determined as a function of the electric vector E orientation. These measurements provide semi-quantitative values of water content but polarized IR spectra with the electric vector E parallel to three principal optical vibration directions will be needed for full characterization and quantitative determinations of water content. After coring, two doubly polished plates were prepared for each feldspar staring material for the final IR absorption measurements, one parallel to (010) to collect polarized IR absorption spectra with OH absorption vibrations in principal optical directions α and β, and one that is either parallel to (001) or (201) (depending on the geometry of the crystal) to measure OH absorptions in the γ optical direction. These IR plates will ultimately be measured by IR spectroscopy and OH bands characterized quantitatively using a Bruker Vertex 70 FTIR spectrometer of the Jacobs Research IR laboratory operated by Dr. Anne Peslier (Johnson Space Center, Houston, TX). Hydrogen speciation will be determined for the starting crystals, based on OH band assignments to OH and H_2O point defects, molecular water clusters, and fluid inclusions (Beran, 1986; Kronenberg et al., 1996; Johnson and Rossman, 2003; Mosenfelder et al., 2015). Integrated OH absorbances, summing over α, β, and γ directions, willbe determined by methods described by Mosenfelder et al. (2015) and used to precisely calculate initial OH contents. These determinations must await the reopening of the NASA Johnson Space Center laboratories. Preliminary IR spectra of the sanidine crystals

suggest they are very dry, while the Baveno crystal exhibits a large OH band similar to those of wet sanidine crystals. TheAdularia selected for this study has modest-size OH bands that appear at identical wavenumbersto those in spectra published for microcline and adularia. The ordered microcline and perthitic microcline selected for this study exhibit large unpolarized OH absorption bands due to fluid inclusions, rather than hydrous point defects.

2.2. Deformation Experiments

Triaxial compression experiments were performed on right circular cylinders of feldspar, 0.400±0.035in (10.16±0.889mm) in length and 0.195±0.002in (4.953±0.05mm) in diameter, using a Griggs solid-medium piston-cylinder apparatus (Figure 7). These experiments are designed to activate dislocation glide on the (010) [001] and (001) 1/2[110] slip systems by deforming the crystals in the [012] direction (Willaime and Gandais, 1977; Willaime et al., 1979). The sanidine single crystals deformed in the [001] direction were prepared to activate the $(12\bar{1})[101]$ slip system with a Schmid factor of 0.477. The compressive differential stress (σ_1 - σ_3) in excess of confining pressure (Pc = σ_3) was applied along sample cylinder axes, with large shear stresses resolved on these slip systems for each experiment (Schmid factors are nearly 0.5 for all three systems). Samples were deformed using a solid-salt piston-cylinder cell (Figure 7b) and methods described by Holyoke and Kronenberg (2010). The Griggs apparatus employs two pistons, one to apply a confining pressure at lateral cylindrical sample surfaces by advancing a confining pressure piston (labeled σ_3), relying on the low strength of NaCl at elevated temperatures to approximate isostatic conditions, and a second piston to apply an additional load at the ends of samples by advancing a load piston (labeled σ_1) at a constant displacement rate (Figure 7b). Axial forces are measured using a load cell of the Griggs apparatus, which is external to the pressure vessel. Thus, load

records require corrections to remove frictional resistance at load piston packings, and viscous losses in upper, colder portions of the sample assembly. Force records were corrected using values of force measured upon the first contact of the sample (referred to as the "hit point"), and the stress correction of Holyoke and Kronenberg (2010). Calibration correction is less precise at low strain, resulting in a kink in the initial linear elastic response during stepping tests. No correction was made for elastic recovery of stepping tests. Stresses were corrected for the changing cross-sectional area of samples undergoing axial shortening, assuming constant sample volume. Samples were shortened at constant axial strain rates ($1.6 \times 10^{-6} s^{-1}$ to $2.1 \times 10^{-4} s^{-1}$) using a constant speed motor mounted at the top of the load frame (Figure 7a). Sample strain measurements and strain rates were determined using displacement transducer (DCDT) measurements of axial displacement (l-l_o) normalized by initial sample length, l_o. Strain measurements were corrected for distortion of the apparatus pistons and load frame (Appendix # data files). Elevated temperatures are achieved using a resistive graphite furnace and temperature is monitored by either a sheathed K-type (chromel-alumel) thermocouple (up to 800°C) or an S-type (platinum-rhodium) thermocouple (at any of the experimental temperatures). For experiments at T>800°C, each sample is encased in a Ni sleeve (wall thickness of 0.6 mm) inside of an annealed Pt jacket (wall thickness of 0.25 mm). For temperatures below 800°C, samples are encased in Ag foil inside of an annealed Ag jacket. Thin (0.025 mm) annealed Ag or Pt shims are placed at sample ends to reduce shear stresses at sample ends in contact with Al_2O_3 pistons. No correction was made for the strength of the Ag, Ni, and Pt jackets since strengths of the jackets fall within the stress resolution of the Griggs apparatus (±30 MPa). Significant improvements have been made to triaxial piston-cylinder deformation methods since the experiments of Willaime and Gandais (1977) and Willaime et al. (1979). Our apparatus, sample cell, and methods allow differential stress, confining

pressure, and temperature measurements with far greater accuracy and precision than was possible for the early sanidine deformation experiments.

Stress – strain measurements were collected for all starting materials in individual constant strain rate and confining pressure experiments conducted at temperatures of 700ºC and 900ºC. A temperature-stepping experiment was conducted on perthitic microcline by reducing the temperature in steps of 50 to 100ºC. A strain-rate stepping experiment was also conducted on the perthitic microcline by increasing strain-rate between 10^{-6} to 10^{-4} s^{-1} in 5 steps, then returning to the original strain-rate to test for hit point force reproducibility and test for path dependence of the sample flow strength. Samples were unloaded at the conclusion of each step; a new hit point load was determined for comparison with the first hit point and used to determine the displacement dependence of the load piston friction.

All samples have been compared at their yield point and at 3% beyond the yield point. For those specimens that displayed strain hardening. I determined a hardening coefficient, h; for specimens that displayed a peak in strength followed by strain softening; I recorded the peak differential stress. Differential stresses and strains were determined at final conditions before unloading samples. Comparisons of strength in both temperature stepping and strain-rate stepping experiments were made at a common reference strain. Thermally activated flow laws with power, exponential, and Peierls resistance relationships between strain rate and stress were compared with trends in the mechanical data, and flow law parameters were determined by least squares and nonlinear fitting using OriginPro software.

2.3. Microstructural Characterization

All deformed samples were impregnated with low viscosity epoxy (Epotek 301, 301-1) in order to prepare thin sections without loss of sample material along unloading cracks that open during

depressurization. Thin sections were prepared parallel to the axis of each deformed sample and parallel to the long elliptical axis (Figure 8), with the objective of characterizing deformation microstructures by optical microscopy in plane light (PPL) and cross-polarized light (XPL). Optical microstructures were recorded photographically, including undulatory extinction, deformation bands and lamellae, twins, microcracks, evidence of frictional displacement, and dynamic recrystallization. The deformation microstructures were tabulated for feldspars deformed at different deformation conditions, varying water contents, and crystal symmetry (and associated Al-Si ordering). Selected deformed samples were examined by SEM, employing EBSD to measure changes in crystal orientation associated with optical microstructures and map crystal orientations relative to principal stress directions.

2.4. Infrared Spectroscopy

Preliminary IR spectroscopy of the undeformed feldspar crystals has been used to provide semiquantitative measures of H_2O content and hydrogen species of the feldspar starting materials. Doubly polished plates (~1mm in thickness) of two orthogonal orientations for each feldspar have been prepared for fully quantitative measurements of polarized IR absorption spectra using a Bruker Vertex 70 FTIR spectrometer with orthogonal vibrational ***E*** directions parallel to principal optical directions α, β, and γ of each feldspar. In addition, OH bands of deformed feldspar samples will be measured by preparing two orthogonal IR plates though not in principle directions, due to deformation orientation constraints. While these measurements can be used for determinations of total integrated OH absorbances (Mosenfelder et al., 2015) and quantification of changes in water content, they will not be optimal to quantify changes in polarization that might result during deformation. IR spectral measurements of the deformed samples will be made excluding epoxy-filled cracks from the measurement volumes by way of

an aperture (and use of a Hyperion 3000 IR microscope of Jacobs Research, NASA-Johnson Space Center) capable for high spatial resolution (50 μm) measurements. Moreover, IR measurements of polished epoxy blanks made for each batch of impregnating epoxy will allow absorption bands due to epoxy filled cracks to be subtracted effectively. IR spectra and water contents of the deformed samples and undeformed feldspar crystals will be compared to check for any changes in H2O concentration and hydrogen speciation during deformation at elevated temperatures. IR spectra will also be measured for samples that have been heat-treated at T=800oC in air in order to drive off water and hydrous defects prior to deformation experiments. Due to orientation and size constraints, it will not be possible to measure OH absorption bands in optimal, principal vibrational directions. However, the calibration of Mosenfelder et al. (2015) is valid for total integrated OH absorbances, summing over any three orthogonal vibration directions, even if they are not the principal optical directions of the crystal. The different types and concentrations of hydrogen defects of the potassium feldspar starting materials will be correlated with mechanical stress-strain data and predominant deformation mechanisms to quantify the effect of water on plastic strength and mechanisms of deformation. For potassium feldspar samples of similar water content but differing crystal symmetry, any differences in mechanical properties will be inferred to be due to Al-Si ordering.

3. RESULTS

3.1. Mechanical Response

All potassium feldspar samples deformed in this study show similar initial elastic response followed by crystal plastic deformation, with a yield point defined by the departure from linear stress-strain behavior. Differential stresses measured during the experiments are low relative to confining pressure. Replotting principal stresses σ_1 and σ_3 in Mohr space (with axes of shear stress vs normal stress) and the measured orientation θ of sample-scale cleavage fractures from the maximum principal σ_1 orientation, frictional sliding would need to occur at very low resolved shear stresses and high normal stresses (Figure 9 a, b) with friction coefficients of only ~ 0.15. Even though sample-scale cleavage cracks may form readily in fragile single crystals at low mean stresses while increasing pressure Pc in the solid salt cell of the Griggs apparatus, further frictional slip at high Pc would seem to be unlikely, given that friction coefficients for feldspars are $\mu \sim 0.65$ (Byerlee, 1978; Masuda et al., 2019). However, microcracks with close microstructural associations with patterns of undulatory extinction, deformation bands and deformation lamellae indicate that some brittle cracking accompanied plastic flow at high temperatures and pressures.

All microcline, adularia, and baveno samples were deformed in the [012] direction; sanidine single crystals were deformed in the [001] direction. Feldspar crystals deformed at T = 700ºC, Pc = 1.5 GPa and = $1.65*10^{-6}$ s^{-1} yield at stresses from 204 to 613 MPa, while those deformed at 900ºC at the same pressure and strain rate, yield at 132 to 227 MPa (Figures 10 and 11). Following yield, the majority of samples show strain hardening, several samples exhibit nearly

constant stresses at 700ºC and 900ºC of 700 MPa and 180 MPa, respectively, and a few feldspar crystals exhibit a peak stress, followed by gradual strain softening to shortening strains of up to 20%. The stress-strain results of all deformation experiments at yield and selected post-yield shortening strains are listed in Table 3, including those for which the experimental conditions, temperature, pressure and strain rate were held constant, and two stepping experiments, during which strain rate or temperature was stepwise changed, holding other conditions constant. In the following, mechanical results are presented for end-member potassium feldspars according to their crystal symmetry and Al/Si ordering, initial water content, and presence of perthitic albite lamellae, and fluid, mica, and quartz inclusions.

Clear, disordered sanidine samples of monoclinic C2/m symmetry shortened in the [001] direction to activate the $(12\bar{1})[101]$ slip system with a Schmid factor of 0.477. Both samples yield and deform plastically to significant axial strains (ε to ~20%) at differential stresses (σ_1 - σ_3) lower than the confining pressure ($P_c = \sigma_3$) at P_c = 1500 MPa and $\dot{\varepsilon}$ = 1.5-1.8*10^{-6} s^{-1} (Figure 10, a). SFP1-1 (SF-1) shortened within 15° of the [001] direction and deformed at T=700ºC, exhibited a yield stress of 613 MPa, reaching a peak differential stress at 718 MPa soon after yield (at $\dot{\varepsilon}$ = 3.4 %), followed by strain softening to a shortening strain of 17% when the experiment was terminated (Figure 10, a). SFP2-2 (SF-2) was shortened in the [001] direction, deformed at T=900ºC, yielded at a stress of only 135 MPa, and continued to deform at low differential stress (just 175 MPa at a shortening strain of 2.5%) (Figure 10, a). SFP2-2 exhibited strain hardening to strains of nearly 20% with a hardening coefficient h of 219 MPa, as defined by the slope, h (Eq. 1)

$$h = \frac{d(\sigma_1 - \sigma_3)}{d\varepsilon}$$

Remarkably, both of these sanidine crystals deformed by crystal plastic mechanisms, even though their internal water contents are low (~17-18 molar ppm H2O per formula unit feldspar) (Table 2); water contents for which quartz single crystals would remain strong and brittle (Kronenberg, 1994).

Clear baveno potassium feldspar samples with large OH absorption bands that are comparable to those of Eifel sanidine crystals (Mosenfelder et al., 2015) exhibited yield strengths at T = 700º and 900ºC (584 and 140 MPa, respectively; Figure 10, b) at Pc = 1500 MPa and $=1.6*10^{-6}$ s^{-1} that are similar to those of sanidine crystals deformed in this study. The symmetry and Al/Si ordering of this starting material has not been determined, though EBSD Kikuchi line patterns were readily indexed assuming monoclinic C2/m symmetry. BR-1 reached nearly steady-state stresses of 700 MPa while BF-2 exhibited flow stresses of ~ 180 MPa and mild strain hardening (h = 396 MPa) (Figure 10, b). The OH band exhibited by this feldspar corresponds to OH substitutions for K on large cation sites of sanidine (Mosenfelder et al., 2015), but at much larger concentrations (~4950 molar ppm H2O per formula unit feldspar, Table 2) than determined for sanidine starting crystals.

Clear, ordered adularia samples with transitional monoclinic-triclinic symmetry (macroscopically C2/m and triclinic C1 micro-domains) deformed at T=700ºC and 900ºC exhibited similar yield strengths at the two temperatures (204 and 227 MPa, respectively), much lower than yield strengths of sanidine, baveno and disordered potassium feldspars crystals deformed at T=700ºC. Adularia experiment, AF-1, at 700ºC showed strain hardening after yielding (Figure 10, c), initially with a hardening coefficient h of 848 MPa (strains of 5-10%) and then by a lower hardening rate of h = 142 MPa (strains of 10-20%), ultimately reaching a differential stress of nearly 326 MPa at ~19.6% strain. Adularia, AF-2 deformed at T=900ºC

reached a peak stress of 381 MPa following the yield point and then showed strain softening, reaching a nearly steady differential stress of 260 MPa at ~20% strain. The low plastic strength of adularia at the lower temperature may be related to hydrous defects in this crystal revealed by OH bands assigned to individual H_2O molecules on K sites with concentrations of 615 ppm (H2O per formula unit feldspar, Table 2) .

Red perthitic microcline samples of low symmetry (C1) and high water-content (2380ppm) due to abundant fluid inclusions (Table 2) deformed at the same conditions as higher symmetry samples exhibit similar mechanical responses. Perthitic microcline (PF) samples shortened at P_c=1500 MPa, and $\dot{\varepsilon}$=1.6 - 2.0*10^{-6} s^{-1} yield at differential stresses of 550 MPa and ~173-184 MPa at T=700° and 900°C, respectively (Figure 11, a). PF-5 deformed at T=700°C reached a peak stress of 608 MPa soon after yielding, followed by strain softening to a final stress of 452 MPa at 19% strain before the experiment was terminated. PF-2 reached nearly steady state stresses of 180 MPa while PF-7, which was annealed at 800°C for a week prior to deformation, shows nearly linear strain hardening with a hardening coefficient of h=388.7 MPa (Figure 11). White microcline samples, consisting of low symmetry (C1), ordered potassium feldspar with solid inclusions of albite, quartz, muscovite and large water contents (2210 ppm; Table 2) in the form of fluid inclusions exhibited peak flow strengths and strain softening (Figure 11, b). Both experiments MF-1 and MF-2 were deformed at T=700°C at a strain rate of 1.6*$10^{-6}$$s^{-1}$ and Pc=1500MPa; higher temperatures were not tested to avoid melting of these altered, micaceous samples. MF-1 exhibited a yield stress of 544 MPa before reaching a peak stress at 701 MPa and 5.6% strain, followed by strain softening to a final stress of 517 MPa ($\dot{\varepsilon}$ = 19.2%). MF-2 exhibited a yield stress of 483 MPa and a peak stress of 556 MPa at $\dot{\varepsilon}$ = 5.3%, before strain softening to a final stress of 259 MPa at 19% strain.

The significant influence of temperature on differential stresses measured for potassium feldspar crystals at a constant strain rate and the large strains accompanied without rapid decrease in stress imply that crystal plastic deformation mechanisms were important and that thermally activated flow laws govern deformation. I therefore conducted two triaxial deformation experiments on perthitic microcline samples, imposing stepwise changes in strain rate and in temperature, with the objective of evaluating the stress, strain rate, and temperature relations for its crystal plastic deformation.

3.2. Strain Rate Stepping Results

The strain rate stepping experiment PF-6 conducted on perthitic microcline at T = 900°C and Pc = 1500 MPa compares favorably with single-condition experiments performed at the same temperature and the sample selected strain rate. The results plotted in Figure 12 show increasing differential stress with stepwise increases in strain-rate (Table 3). The results of the first step of PF-6 conducted at $\dot{\varepsilon}=1.6*10^{-6}$ s^{-1} compares favorably with the individual experiments PF-2 and PF-7 on the same starting material at the same strain rate.

With each sequential increase in strain rate of PF-6, yield stresses increase, from 132 MPa of the first strain rate, $\dot{\varepsilon}=1.6*10^{-6}s^{-1}$ to 248 MPa of the highest strain rate, $\dot{\varepsilon}=2.7*10^{-4}s^{-1}$. Rates of strain hardening are comparable (h=313-534 MPa) at all but the highest strain rates (h=785 MPa at $\dot{\varepsilon}=2.7*10^{-4}s^{-1}$), with flow strengths of 175 to 325 MPa measured at 3% strain beyond each yield point. After increasing strain rate with each step of this experiment, the sample was tested at the original displacement rate, and somewhat larger strain rate than that of the first step ($\dot{\varepsilon} = 2.7*10^{-6}s^{-1}$) owing to the reduced sample length at the beginning of the final step. While the yield and flow strengths (at 3% beyond yield) measured during this final step are lower (42 and 86 MPa)

than those determined for the first strain rate imposed, the reduction in strength following the high strength – high strain rate deformation, and reduction in hardening rate (h=199 MPa at $\dot{\varepsilon}$ =2.7*10^{-6}s^{-1}) suggest a measure of reversibility of the flow law for perthitic feldspar. Of the strengths determined at 1.6-2.7*10^{-6}s^{-1} of this experiment, I am more confident of stresses measured during the first strain rate step, given that strains accumulated during this experiment (to 55% shortening) can lead to uncertainties in true cross-sectional area of the originally cylindrical sample. Compiling the flow strengths (at 3% post-yield strains) as log(σ_1-σ_3) vs log($\dot{\varepsilon}$), a clear trend is defined between strain rate and flow strength (Figure 13).

3.3. Temperature Stepping Results

The temperature-stepping experiment PF-4 conducted on perthitic microcline at $\dot{\varepsilon}$ = 1.7-2.9 *10^{-6}s^{-1} and Pc=1500MPa confirms the dependence of plastic flow strengths of the perthite and other potassium feldspars on temperature (Figure 12, Table 3). With each sequential decrease in temperature of PF-4, yield stresses increase from 176 MPa of the first imposed temperature T=950^{o}C to 557 MPa of the final temperature T=650^{o}C. Rates of strain hardening, h, range from 311 to 786 MPa over temperatures of 950^{o} to 700^{o}C, while hardening is greater (h=1426 MPa) at the lowest temperature (T=650^{o}C). Flow strengths of PF-4 measured at T=700^{o}C and 900^{o}C (434 and 196 MPa at 3% post-yield strains, respectively) compare favorably with flow strengths measured in single-condition experiments on perthitic microcline (Table 3) with an even lower flow strength measured during the first T=950^{o}C step and the highest flow stress (and hardening rate) measured for the final T=650^{o}C step. Compiling the flow strengths (at 3% post-yield strains) as log(σ_1-σ_3) vs 1/T where T is in K, a clear trend is defined for the thermally activated

plastic flow of perthitic microcline (Figure 13). This trend is displayed best by the temperature-stepping results of PF-4, but it is also corroborated by individual experiments performed at T=700ºC and 900ºC, even though these results also include sample-to-sample variations.

3.4. Comparison of Results for Potassium Feldspars of varying Symmetry, Ordering and Hydrous Defects

Our potassium feldspar samples were chosen for the wide range of crystal symmetry, Al/Si ordering, and differing hydrous defects, fluid inclusions and solid inclusions. The similarity of mechanical properties of these different potassium feldspars is striking in light of differencing unit cells, crystal structure, and defects. My samples include the highest symmetry of any feldspar, monoclinic C2/m sanidine with disordered Al/Si through the transitional monoclinic-triclinic symmetry of adularia and baveno and the low symmetry, C1, microcline samples with ordered Al/Si. The types of water in the starting materials range from H_2O inclusions in microcline, to individual H_2O molecules on K sites in adularia and OH defects occupying K sites in baveno and sanidine crystals. The water concentrations vary from 17 ppm to 4950 ppm. The range of water in these feldspars is comparable to the range of water contents of synthetic quartz crystals (Kekulawala et al., 1981) over which large variations in flow strength are readily measured. Studies of polycrystalline feldspars suggest a strong correlation between amount of water and material strength. Such strong effects of hydrous defects and water on single crystal plasticity of potassium feldspars are not apparent in this study.

3.5. Observed Sample Strains

Following the deformation experiments, the samples, still in their metal jackets appear uniformly shortened and lateral dimensions as seen at specimen ends are visibly elliptical owing to the two

principle slip systems activated by shortening in the [012] direction and one principle slip system activated by shortening in the [001] direction leading to nearly plane strain (Figure 14, 15). Thin sections prepared parallel to the original cylindrical axis and parallel to the long elliptical axis of deformed samples (Figure 8) provide observations of cleavage cracks, undulatory extinction due to the principal slip systems and mechanical twinning . They can further be used to verify along-axis shortening strains and lateral strains during the experiments. Final sample dimensions observed for jacketed (Figure 14, 15) and whole sample thin sections are listed in Table 4.

3.6. Microstructures

All deformed feldspar samples show extensive undulatory extinction in crossed polarized light, microcracks that are fully contained within the single crystals, and twins (with the exception of BF-1) (Figure 16, 17). Some twins in deformed microclines (PF, MF) might represent original twins of the starting material (Figure 6); yet some may have formed during deformation. Sample- scale fractures with cleavage orientations may have formed during pressurization, given that similar fractures are present in the sample MF-L pressurized to Pc=1500MPa but not explicitly shortened by the σ_1 load piston (T=300ºC, SSA, standard experimental procedures); (Figure 17, f). Cleavage fractures are ideally oriented for frictional sliding under the sample assembly loading conditions and low mean stresses. The shear displacements of these fractures (204 – 550 μm) are comparable to those of the pressurized sample (442 μm) and may not have contributed much to sample strain at the high mean stresses of the triaxial experiments. In contrast, many of the microcracks present in deformed samples appear to have formed by transitional brittle-plastic mechanisms during deformation. Many of these cracks range from parallel to subparallel to sample axes, and commonly show microstructural relationships with deformation bands, patterns of undulatory extinction, fluid inclusions and deformation lamellae

that suggest simultaneous activation with crystal plastic processes. Some microcracks are oriented perpendicular to specimen axes and cannot have opened under the triaxial stress conditions of the experiments.

These microcracks are assumed to have formed during the unloading stage after deformation. Identification of cross-cutting relationships is critical to the evaluation of cracks that formed and facilitated shear displacements during the experiments and evaluation of those formed during depressurization that did not contribute to the measured mechanical behavior.

In the following, I describe all deformation microstructures that developed at the high pressure and temperature experimental conditions; describing cross-cutting relationships, and referring to demonstrable extension cracks due to depressurization only when necessary to identify their occurrence in micrographs, and distinguish them from deformation microstructures that can be linked to the measured mechanical response of feldspar. Descriptions of cleavage fractures and microcracks with orientations that promote significant shear stresses at triaxial stress conditions are included here, making sure to include observations that suggest their formation during pressurization or during the experiment.

Whole sample micrographs of sanidine, baveno, and adularia samples deformed at T = 700ºC and T = 900ºC display patterns of undulatory extinction and sample-scale cleavage fractures that likely formed during pressurization but served to localize deformation by a combination of dislocation slip, microcracking, and mechanical twinning (Figure 16). The sanidine crystal deformed at Pc=1.5GPa, $\dot{\varepsilon}$= $1.65*10^{-6}s^{-1}$, and T = 700ºC (SF-1) exhibits one large crack surrounded by localized undulatory extinction and microcracks that are overprinted by extensional cracks due to unloading. The brittle microcracks and surrounding crystal plasticity have geometrical relationships that suggest their simultaneous activation at experimental

conditions (Figure 18). Patterns of undulatory extinction appear to be related to thoroughgoing fractures are localized near these fractures (Figure 18, a). The sanidine crystal deformed at Pc=1500 MPa, $\dot{\varepsilon}$=1.8*10^{-6}s^{-1} and T = 900ºC (SF-2), exhibits sweeping undulatory extinction that defines broad regions of crystal plasticity and external rotation of crystal axes, fine-scale deformation lamellae, fine bands of undulatory extinction, and microcracks, with local regions of strong undulatory extinction. Fine-scale deformation lamellae are well expressed along (121) slip planes within the broad diagonal deformation band of sample SF-2, due to variations in refractive index (presumably due to high defect densities); (Figure 19). These lamellae are visible in cross-polarized light as well as in plane light, and are accentuated by dialing down the condenser aperture to increase optical relief (Figure 19). Remarkably, fine-scale fluid inclusions (1 um) are visible, localized on deformation lamellae implying interaction between trace hydrogen defects, inclusions and dislocations, despite the broad-beam IR measurements of sanidine starting crystals that reveal only small OH concentrations (17 and 18 ppm molar H2O per formula unit feldspar). SF-2 was deformed in the [001] direction and effectively activated the $(12\bar{1})[101]$ slip system with a Schmid factor of 0.477. Exhaustive optical microstructural analysis of these samples also failed to reveal subgrains or subgrain walls. While the complexity of cleavage cracks and microcracks offer challenges to interpret their timing and contributions to the high pressure, high temperature deformation, the presence of undulatory extinction and deformation lamellae indicate crystal plasticity was important during the experiments. The clear, yellow sanidine starting materials for these experiments show straight extinction in thin section prior to deformation with no evidence of twins, exsolution lamellae or microcracks.

Deformed baveno-growth feldspar samples show extensive evidence of both brittle fracture and crystal plastic mechanisms (Figure 20, a; Figure 16, c, d; Figure 14, c, d; Figure 21, a; Table 4)

with microstructural relationships that indicate simultaneous brittle - plastic deformation. Whole-sample observations of the baveno feldspar deformed at T=700ºC (BF-1) offer challenges to understanding both the mechanical results and microstructures of this experiment. While cores prepared from a cluster of large baveno-growth crystals were intended to consist of individual single crystals, this sample includes a large original twin (Figure 21 a). As a result, the mechanical results reflect the properties of a bicrystal with most of the sample in the desired orientation, but with a significant volume fraction of the sample oriented poorly for dislocation slip. Deformation microstructures of this sample are complex. In contrast, the microstructures of the baveno-growth sample deformed at T=900ºC (BF-2) are straightforward, with cross-cutting cleavage fractures throughout the sample and undulatory extinction due to crystal plasticity localized along the fractures (Figure 16, d). Although the baveno-growth crystal contains naturally sealed cleavage cracks with secondary minerals precipitated within the natural cracks, their presence in the starting material did not affect deformation much. The sealed cleavage cracks display minor tensile cracking of the secondary mineral within the feldspar (Figure 20, a) but additional brittle deformation of the host feldspar around these secondary phases is not apparent. Brittle cracking and undulatory extinction associated with plastic deformation is localized and associated with the large, parallel cleavage fractures that transect the sample (Figure 16, d).

Deformed adularia crystals show microstructures that indicate both brittle and plastic deformation was important at experimental conditions. Undulatory extinction, microcracks and twins are visible in both AF-1 and AF-2 (Figure 16, e,f; Figure 14, e,f; Table 4). The low temperature (T=700ºC) adularia (AF-1) sample includes twins and undulatory extinction localized near fractures, and newly recrystallized feldspar grains (~22μm) are observed along

complex and highly deformed fracture zones (Figure 20, b). Fluid inclusions are present throughout the sample, aligned in planes, particularly near heavily fractured regions (Figure 20). Adularia, AF-2 deformed at T = 900°C contains twins, which are localized at sample ends, occasional kink bands that distort twins, and recrystallized grains (~12-14μm) along complexly deformed fractures (Figure 20, c).

The microstructures of deformed microcline samples (PF, MF) are significantly more complicated than those of higher symmetry, disordered varieties of potassium feldspar, due to the natural occurrence of exsolution lamellae and inclusions of albite. Tartan twinning, which is pervasive in both microcline starting materials (Figure 17, Figure 6), is altered in the deformed samples. Albite lamellae and inclusions of the starting material are complex (Figure 21, b, c, e) but they also serve as strain markers. All deformed red perthite samples contain brittle – plastic deformation microstructures, changes in microcline twinning, and fluid inclusions (Figure 17 (a, b, c), Figure 21 (b, c)). The (001) plane is particularly important in microcline deformation experiments as a dominant slip plane, twinning orientation, and perfect cleavage plane. The importance of this principle plane is supported by Woensdregt (1982) who determined (001) is an F1 face parallel to at least two periodic bond chains (PBC) (Woensdregt, 1982). Both PF-5 and PF-7 perthitic microclines show sample-scale cleavage fractures with comparable displacements (204 and 387 μm, respectively) to that of the pressurized sample MF-L (442 μm). Brittle microcracks localized within albite lamellae are present in all samples but they are most prominent in single condition experimental samples, PF-2, PF-5, and PF-7. These microcracks form along the (001) cleavage plane in albite and do not propagate into surrounding microcline (Figure 22, b). The termination of microcracks at the lamellae boundary could be due to the slight misorientation between albite and microcline, where the two (001) cleavage planes are not

perfectly aligned (Figure 21, c, d). Displacements along albite cleavage microcracks are visible in all samples but most prominent in the low temperature PF-5 and annealed PF-7 samples (Figure 22). The interaction between brittle albite microcracks and plastic processes in the surrounding microcline is apparent at crack tips where stress fields of the cracks correspond to undulatory extinction that fans out from the crack-tips and albite-microcline lamellae boundaries (Figure 22, b). These brittle-plastic microstructural associations provide strong evidence of simultaneous activation and interaction of frictional slip on microcracks and dislocation slip (Figure 22, b). Localized microcracks and deformation lamellae within albite lamellae routinely intersect planes of fluid inclusions along the albite-microcline boundary (Figure 22, d). In some cases, these cracked zones are observed in the absence of albite exsolution lamellae. The deformed zones of this character, where the feldspars composition is homogeneous, are narrow (<20μm); wider zones of brittle-plastic microstructures continue to be associated with wide lamellae of albite. These microstructures will be addressed in the discussion associated with the homogenization of alkali feldspar at experimental conditions (Figure 22, d).

Planes of fluid inclusions are common throughout all perthitic microcline samples, both in the starting material and in deformed samples, serving in the formation of large fractures. In the two high-strain temperature- and strain rate-stepping experiments, PF-4 and PF-6, planes of fluid inclusions appear to facilitate recrystallization (~19μm)(Figure 22, f). Recrystallization along large fracture surfaces is present in all perthite samples with newly formed grains of varying size (<17μm) (Figure 22, a, e).

Deformation lamellae are present within all deformed perthite samples, particularly within the albite lamellae (Figure 23, identification technique shown in Figure 19). In Figure 23, thin parallel deformation lamellae are clearly visible, within planar orientations that are 10-17^{o} from

those of cleavage microcracks. Both microcracks and deformation lamellae terminate at the microcline-albite lamellae boundaries (Figure 23) where fluid inclusions are concentrated. The original tartan twins of microcline are replaced by a simple set of coarse albite twins in the low temperature perthitic microcline (PF-5, T=700ºC). Original tartan twins found in the PF starting materials are absent in both high temperature samples (PF-2, PF-7, T=900ºC), replaced by domains of slight undulatory extinction. Perpendicular albite and pericline twins are observed only at one end of the PF-7 sample. These tartan twins may be relicts of the original twinning or were more likely reestablished during deformation. With this exception, tartan twins are absent from the high temperature experiments on PF. Crystallographic axes determined by EBSD, reveal a single consistent orientation of untwinned potassium feldspar.

White microcline samples deformed at T = 700ºC, Pc=1500 MPa, and $\dot{\varepsilon}$ = 1.7-1.8 *$10^{-6}s^{-1}$ (MF-1, MF-2) exhibit undulatory extinction along fractures (Figure 24, a)(Figure 17, g, h), microcracks, twins, and kink bands, with little evidence that potassium feldspar strain patterns are controlled by isolated solid inclusions of albite, quartz, or mica. Isolated quartz inclusions appear undeformed and even weak mica inclusions with deformation-induced kink bands do not appear to affect the host-microcline deformation microstructures (Figure 24). However, mica grains that have coalesced form a continuous gouge layer along a major sample-scale fracture of deformed microcline MF-2 (Figure 24 a and c). Micas within this fracture display a S-C fabric consistent with the sense of shear. While the mica-lined fracture of this sample has a similar orientation relative to the sample axis as the pressurized sample MF-L (Figure 17), the shear displacement of the mica-lined fracture of deformed microcline MF-2 (1050 μm) exceeds that of MF-L (442 μm). Localized shear displacement due to micas along this fracture appears to have been significant during triaxial compression, owing to the low frictional strength of mica.

3.7. Flow Laws

While all potassium feldspar crystals deformed in this study exhibit both brittle and plastic microstructures, the strong temperature and strain rate dependencies of strength suggest dislocation glide and potential recovery processes are important at temperatures of 650°C to 950°C and pressures of 1.5 GPa.

The strain-rate stepping, temperature stepping, and single condition deformation experiments performed on perthitic microclines were used to evaluate potential flow laws, plotting differential stress (σ_1-σ_3) measured at 3% strain beyond the yield point versus the imposed strain rate at a given temperature, and the same stress versus temperature at a given strain rate (Figure 13). Three thermally activated flow laws were chosen, with strain rate – stress relationships described by a power law, an exponential law, and a Peierls lattice resistance law (Frost and Ashby, 1982; Poirier, 1985). Physically based, microstructural models of dislocation creep involving the glide and climb of dislocations lead to a thermally activated power law for strain rate, $\dot{\varepsilon}$, in terms of differential stress (σ_1-σ_3) and absolute temperature, T:

$$\dot{\varepsilon} = \dot{\varepsilon}_{o\,PL} \left(\frac{\sigma_1 - \sigma_3}{\mu}\right)^n \exp\left(\frac{-H^*}{RT}\right) \qquad \textbf{Power Law} \quad (2)$$

where $\dot{\varepsilon}_{o\,PL}$ is strain rate at a standard state, μ is the elastic shear modulus of the material, n takes on values of 3 to 5, R is the gas constant, and H* is the activation enthalpy for the rate-controlling step, potentially involving the critical energy barrier of either dislocation slip or diffusion of point defects, dislocation climb and recovery. I adopt the effective, isotropic shear modulus of microcline, μ, from the compilation of Bass (1995), based on experimental measurements of Hearmon (1984). The exponent n was determined by least squares fitting of the power law (eqn. 1) to the $\log(\sigma_1$-$\sigma_3) - \log(\dot{\varepsilon})$ results of the strain rate-stepping experiment

on perthitic microcline (PF-6, Figures 12, a and 13), using statistical functions of OriginPro (see Appendix). Activation enthalpy, H*, was determined by least squares fitting of the temperature- stepping results in $\log(\sigma_1-\sigma_3)$ – 1/T space (PF-4, Figures 12, b and 13). Combining these results with the flow strengths of all perthitic microcline experiments, best-fit parameters of the power law fit are:

$$\log(\dot{\varepsilon}_{o\ PL}) = 23.2 \pm 0.66\ s^{-1}$$

$$n = 7.70\ \pm 0.19$$

$$H^* = 281.7\ \pm 6.7\ \mathrm{k}J/mol$$

$$\mu = 28.1\ GPa$$

While the fit of the power law to the experimental data is excellent (r = 0.99), the deformation microstructures and highly nonlinear relationship of $(\sigma_1-\sigma_3)$ and $\dot{\varepsilon}$ (n > 5) suggest that deformation is governed by dislocation glide with little diffusional or recovery control. Therefore, two other flow laws based on dislocation glide were used to fit the data for perthitic microcline. Dislocation glide in the absence of significant dislocation climb may follow an exponential law:

$$\dot{\varepsilon} = \dot{\varepsilon}_{o\ EL} \exp\big(\alpha(\sigma_1 - \sigma_3)\big) \exp\left(\frac{-H^*}{RT}\right) \qquad \textbf{Exponential Glide Law}\ (3)$$

where $\dot{\varepsilon}_{o\ EL}$ is strain rate at a standard state, α is related to an activation area for glide, and H* is the activation enthalpy for glide. A best-fit value of α was determined by least squares fitting of the exponential law (eq. 2) to the strain rate-stepping data in $(\sigma_1-\sigma_3)$ – log $\dot{\varepsilon}$ space (PF-6, Figures 12, a and 13). The combined results of all perthitic microcline experiments are fit with parameters of:

$$\log(\dot{\varepsilon}_{o\ EL}) = 3.6 \pm 1.4\ s^{-1}$$

$$\alpha = 0.0315 \pm 0.0018 \ MPa^{-1}$$

$$H^* = 281.7 \pm 6.7 \ kJ/mol$$

Alternatively, the dislocation glide of perthitic microcline can be described by the Peierls lattice resistance law:

$$\dot{\varepsilon} = \dot{\varepsilon}_{o\,PR} \left[\left(\frac{\sigma_1-\sigma_3}{\mu}\right)^2\right] \exp\left(\frac{\sigma_1-\sigma_3}{\sigma_p}\right) \exp\left(\frac{-H^*}{RT}\right) \qquad \textbf{Peierls Lattice Resistance Law} \ (4)$$

where $\dot{\varepsilon}_{o\,PR}$is strain rate at a standard state, and two differential stress (σ_1-σ_3) terms appear, one normalized by the athermal Peierls stress, σ_p. Iterative nonlinear fitting (OriginPro, see appendix for details) of the Peierls law (eq. 3) to perthitic microcline data in (σ_1-σ_3) – $\dot{\varepsilon}$ space (Figures 12, a and 13) gives a best-fit value of the Peierls stress, σ_p. The combined results for perthitic microcline experiments are well-described by:

$$(\dot{\varepsilon}_{o\,PR}) = 8.8 \pm 1.2 \ s^{-1}$$

$$\sigma_p = 44.4 \pm 1.2 \ MPa$$

$$H^* = 281.7 \pm 6.7 \ kJ/mol$$

$$\mu = 28.1 \ GPa$$

With residuals between the data and flow law well within experimental stress resolution. The choice of flow law must be made according to the mechanisms responsible for deformation, given that statistical fits of the three flow laws to the data are all satisfactory, within uncertainties of the differential stress (±30 MPa) measurements using the solid salt sample assembly and Griggs apparatus (Holyoke and Kronenberg, 2010). Optical deformation microstructures of all feldspars deformed in this study are dominated by undulatory extinction and deformation lamellae, with little evidence of subgrain wall development, and few recrystallized grains. As a result, the exponential and Peierls flow laws are favored to describe the plastic deformation.

However, both of these laws only describe steady-state deformation; thus, they can only provide approximate descriptions of strain hardening plastic deformation and they cannot describe strain softening. For individual steps of the condition-stepping experiments with little strain hardening (small h), the chosen flow laws provide a first-order description of deformation. Ultimately, transient creep laws may be required to describe plastic flow when stresses become large and values of h are large, determined at high strain rate ($2*10^{-4}s^{-1}$; Figure 12, a) or low temperatures (T=650^{o}C; Figure 12, b), or when strain localization leads to strain softening. Incorporation of brittle cracking and frictional slip must await determinations of sliding rate and temperature-dependent friction.

4. DISCUSSION

The mechanical results of this study are consistent with previous experimental studies of feldspar deformation by semi-brittle and plastic deformation at elevated temperatures and pressures. Differential stresses of potassium feldspar crystals deformed in this study fall in the range of stress measurements for plagioclase crystals deformed by dislocation slip, cracking and mechanical twinning at confining pressures Pc of 500-1500 MPa (Borg and Heard, 1970; Marshall and McLaren, 1977; Stünitz et al., 2003, respectively). Despite the very different compositions and structural states of plagioclase crystals deformed in these earlier studies from the potassium feldspars deformed in this study, differential stresses of 200-300 MPa were measured for plagioclase crystals oriented for dislocation slip at T = 800^{o} and 900^{o}C and strain rates of 10^{-5} - 10^{-7} s^{-1}. Microstructures and defects generated in deformed plagioclases included undulatory extinction, dislocations, microcracks and twins, much as reported here. While previous experimental solid-medium Griggs apparatus methods did not allow Williame et al. (1979) to measure differential stresses reliably, the microstructures they reported for sanidine single crystals deformed at the conditions of my experiments include sample-scale fractures, microcracks, undulatory extinction, and deformation lamellae.

The mechanical results reported here for perthitic microcline compare favorably with experimental results for similar perthitic microclines reported by Negrini et al. (2014) for comparable experimental temperatures, pressures and strain rates. Both the earlier work and this study show an inverse relationship between sample strength and temperature, with high peak differential stresses measured at lower experimental temperatures and relatively constant flow stresses of ~300 MPa measured at higher temperatures (Negrini et al., 2014). All experimentally

deformed perthites show brittle sample-scale fractures, microcracking, and undulatory extinction due to plastic deformation. The primary difference between this study and that of Negrini et al. (2014) is that I restricted my experiments to conditions that avoided melting, while Negrini et al. (2014) added 0.2 wt% water to the metal jackets sealing in the perthite samples, leading to melting at reduced temperatures. One of the goals of this earlier study was to investigate the effect of <5% melt on mechanical properties.

The results of these single-crystal feldspar experiments can also be compared with results of polycrystalline albite deformation experiments (Tullis and Yund, 1980). Flow stresses for polycrystalline albite samples (of 350-1600 MPa) deformed wet and dry at T > 700ºC, confining pressures of 1000-1500 MPa and a strain rate of 10^{-6} s^{-1} are larger than strengths of the potassium feldspar single crystals deformed in this study, as expected for polycrystalline samples in which only a small fraction of grains are well oriented for slip. Deformation microstructures of polycrystalline albite samples included dense microcracks, patchy undulatory extinction, dislocations and densely tangled dislocations due to dislocation interferences.

4.1. Crystal Plastic Mechanisms

Undulatory extinction is present in every deformed potassium feldspar sample. In most samples, the undulatory extinction is patchy and localized near fractures. Close relationships of microcracks with sharp undulatory extinction suggest simultaneous activation of brittle and plastic mechanisms. Variations from patchy extinction to sweeping, sample-wide undulatory extinction, as noted in SF-2, are probably due to local variations in dislocation densities.

Widespread undulatory extinction in this sample suggests that dislocation glide was dominant at T=900ºC and Pc=1500MPa. The absence of optically detectable subgrain walls indicates that recovery and dislocation climb were limited.

The presence of deformation lamellae (Figure 19) along the $(12\bar{1})$ slip plane indicates that slip on the system $(12\bar{1})[101]$ contributed to the deformation. Fine deformation lamellae are found parallel and adjacent to fine, linear bands of undulatory extinction (SF-2). They are also well developed within albite lamellae on (001) of the perthitic microcline samples (PF) (Figure 18; Figure 23). Slip on (010)[001] could have also been important but did not result in optically visible lamellae.

In deformed samples of potassium feldspars that lack microstructures in the starting materials, such as deformed sanidine crystals, twins can be inferred to have formed under the deviatoric stresses of the experiments. However, much of the sample strain must be accommodated by other mechanisms, given that twinning strains of feldspars are small (Starkey, 1963; Borg and Heard, 1969) (Figure 18). In deformed samples whose starting materials are already twinned, (PF and MF), the presence or absence of twins is more complex. Twins in perthitic microcline PF-7 taper at their ends suggesting that these twins formed in shear as opposed to relict twins of the complex starting material.

4.2. Roles of Cleavage and Microcracking

Samples well oriented for slip on (010)[001] and (001)1/2[-110] are also susceptible to frictional sliding on (001) perfect cleavage and (010), cleavage cracks formed while samples were pressurized before high pressures were achieved. Many of the feldspar starting crystals are

fragile with preexisting, naturally formed cleavage cracks. Thus, cleavage fractures can propagate while preparing samples and during pressurization.

To test for cleavage cracking prior to high temperature, high pressure deformation, a sample of white microcline was prepared and pressurized to high confining pressure (at T=300^{o}C) but not shortened triaxially. This sample (MF-L) contains a large sample-scale fracture with 442 μm of displacement (Figure 17) demonstrating that such fractures may have formed under non-hydrostatic stresses applied by the solid salt confining medium before high confining pressures Pc were reached. Thus, sample-scale fractures of deformed samples (PF-4, PF-5, PF-7, BF-1, MF-1, MF-2) may have formed before experimental conditions were achieved, and mean stresses (and normal stresses on cleavage planes) were large.

Of the deformed feldspar samples with sample-scale cleavage fracture, three have displacements (204 to 550 μm) comparable to the pressurized sample MF-L. Two samples, MF-2 and BF-1 accumulated larger displacements of 1050 μm and 1286 μm, respectively (Figure 16 and 17). Deformation of sample BF-1, which included a twin, is complex (Figure 21, a). The sample-scale fracture of MF-2 contains mica gouge and feldspar, and frictional displacement on this fracture may have been facilitated by a lowered friction coefficient associated with the presence of mica (Scruggs and Tullis, 1998). Once cleavage fractures are subject to large normal stresses at a Pc of 1500 MPa of the triaxial deformation experiment, it is unlikely that shear displacements on feldspar cleavage surfaces can continue. Plotting the triaxial stress states of high temperature, high pressure experiments and fracture planes in Mohr space (Figure 9), shear stresses on the fractures are low relative to the normal stresses that cleavage surfaces are subjected to. Frictional shear at these conditions would require a friction coefficient for feldspar $\mu = 0.15$ much lower than reported values $\mu = \sim 0.65$ (Byerlee, 1978; Masuda et al., 2019).

Alternatively, if I adopt a friction coefficient for feldspar cleavage fractures of 0.65 and assume that fluids released from decrepitated inclusions increased pore pressure, Pp = P_{H2O}, decreasing effective pressure (Pe=Pc- Pp), frictional sliding could occur if P_{H2O} reached 1286-1437 MPa (Figure 9, b, c). This condition can readily be dismissed since pervasive feldspar melting is predicted at T≥876ºC for P_{H2O} of even 500 MPa (Yoder et al., 1957 as referenced in Deer et al., 2001). In the absence of any observed melt products in any of the deformed samples, I conclude that frictional sliding on these sample-scale fractures was suppressed by the applied confining pressure Pc=1500MPa. Microstructural relationships of undulatory extinction, kink bands, and mechanical twins and the irregular geometries of the sample-scale cleavage cracks indicate that stress concentrations on the pressure-stabilized cleavages served to nucleate crystal plastic mechanisms at high temperatures and pressure. In addition, fine scale microcracks may have formed adjacent to fracture asperities. These microcracks may also have formed at high temperature and pressure in association with heterogeneous plastic deformation.

4.3. Brittle-Plastic Interactions

Microcracks on (001) cleavage planes are localized within albite lamellae of deformed perthitic microcline samples (PF-2, PF-5, and PF-7) and terminate at albite-microcline boundaries (Figure 22, b). The microcline host of albite lamellae with these microcracks exhibits fan-shaped patterns of undulatory extinction in close association with microcrack tips (Figure 22, b). These observations suggest that the growth and frictional sliding on these fine-scale cleavage cracks coincided with plastic deformation during the high temperature, high pressure conditions of the triaxial compression experiment. While analysis of the larger throughgoing cleavage fractures indicate that deviatoric stresses (and shear stresses resolved on cleavage) were not large enough to overcome frictional forces at the high confining pressures of the experiments, sliding on the

fine-scale microcracks appears to be enabled by plastic deformation at microcrack tips. Likewise, the stress concentrations at microcrack tips facilitated dislocation glide. Combining these observations, the brittle and plastic deformation mechanisms in these experiments appear to have interacted in-sequence as dependent processes, rather than operating as independent processes, much as proposed for brittle-plastic deformation of halite and calcite (Chester, 1988; Fredrich et al., 1989).

Deformed perthitic microcline samples also exhibit parallel sets of (001) cleavage cracks that are no longer than 20 μm, which resemble those in albite exsolution lamellae of the same sample (Figure 22, d). The optical character of the feldspar with these crack arrays is uniform, suggesting no changes in composition and the absence of albite exsolution lamellae.

4.4. Potential Roles of Symmetry, Al-Si Ordering, and Exsolution Lamellae

Although the potassium feldspar crystals chosen for deformation vary in symmetry and degree of Al-Si ordering, from monoclinic disordered sanidine to transitional monoclinic-triclinic adularia, to triclinic ordered microclines, the mechanical properties measured at T = 700ºC and 900ºC are remarkably similar. According to equilibrium evaluations of potassium feldspar unit cells and ordering (Smith and Brown, 1988; Deer et al., 2001) all samples deformed at T = 700º-900ºC could have experienced increases in symmetry from triclinic to monoclinic cells and redistribution of Al and Si across T1 and T2 tetrahedral sites. However, the kinetics of Al and Si diffusion are known to be slow, and rates of Al-Si exchange between tetrahedral sites, are significant only at high pressures when water is present (Yund and Tullis, 1980). Thus, some retention of Al - Si ordering at experimental conditions could be retained. Only preliminary

experiments have been done to determine rates of Al - Si disordering in potassium feldspar, but albite can be disordered in 20 hours at 1080ºC (Zhang et al., 1997).

More direct evidence for disordering in my samples during deformation comes from the optical observation that original tartan twins of the deformed microcline samples disappear (Figure 6 and 17 b, c, d). Tartan twins consist of nearly orthogonal sets of intersecting albite (010) and pericline (001) twins, which form during slow cooling of coarse feldspars in subsurface granitic rocks, as a high-temperature monoclinic sanidine structure becomes ordered and collapses to a triclinic microcline structure, while minimizing changes in original grain shape (Deer et al., 2001). Albite twins of tartan-twinned microclines form as temperatures decrease as the newly triclinic lattice retains the same (010) orientation as the original monoclinic (010). Pericline twins form during cooling, maintaining the same a-axis orientation in the newly triclinic lattice as the monoclinic a-axis (Deer et al., 2001).

The loss of original tartan twins of perthitic microcline deformed at T = 700ºC (PF-5), with only albite twins remaining thus indicates that Al - Si disordering resulted in an increase in crystal symmetry. The loss of all original twins of perthitic microclines deformed at 900ºC (PF-2, PF-7) indicates further Al - Si disordering and increases in symmetry at higher temperatures. If all microcline of these samples returned to their original monoclinic structures due to disordering at the conditions of deformation, the tartan twins observed at one end of sample PF-7 may represent mechanical twins formed during deformation, or newly quenched, locally triclinic microcline. More generally, these observations suggest that the mechanical results for even the most ordered potassium feldspar starting materials reflect the properties of high symmetry feldspar due to Al - Si disordering during the experiments. This, in part, helps to explain the

remarkable similarity of plastic flow strengths of the wide array of feldspars deformed in this study.

Microstructures of perthitic microclines also suggest that these complex feldspars underwent homogenization of fine-scale exsolution lamellae (< 15 μm in dimension), much as observed by Negrini et al. (2014). Rates of K and Na self-diffusion and of K - Na interdiffusion in alkali feldspars are much higher than those of Al or Si diffusion (Lin and Yund, 1972; Yund and Tullis, 1980; Brady and Yund, 1983). This explains the occurrence of parallel (001) cleavage cracks in homogeneous potassium feldspar, which I infer to have formed when albite lamellae were still present, while undulatory extinction emanating from these crack tips reflect deformation of the surrounding potassium feldspar before and during diffusional homogenization. Even while narrow albite lamellae were digested during deformation, coarse albite lamellae of the perthitic microcline remain, given that diffusion length scales for homogenization are too large.

4.5. Roles of Mica and Quartz Inclusions

Turbid natural feldspars commonly exhibit fine layer silicate and quartz inclusions due to weathering and retrograde sericite-forming reactions. Multiple studies show that formation of phyllonite shear zones within quartzofeldspathic rocks involves the replacement of strong feldspars by weaker layer silicates (Evans, 1988; O'Hara, 1988; Hippertt, 1998; Bhattacharyya and Mitra, 2011; Farkasovsky et al., 2016). The mica and quartz inclusions of white microcline samples deformed in this study represent the first steps in common retrograde reactions, and once formed, may serve as the nucleation sites for localized shear zones. The results of this study suggest that the distribution of the secondary product phases of weathering reactions is important. While little or no localized deformation is noted in the microcline host surrounding

isolated inclusions of mica and quartz (Figure 24, b), plastic deformation of feldspar is replaced by frictional slip on a mica-rich shear zone in sample MF-2, when micas are contiguous and coalesce through deformation, ultimately leading to a mica-rich gouge (Figure 24). Quartz is generally regarded as weaker than feldspar, both in laboratory experiments (Dell'Angelo and Tullis, 1996) and in natural shear zones. Thus, it is surprising that quartz inclusions within the white microcline were not visibly deformed, nor is deformation of the microcline host visibly affected. Further evaluation of this observation will have to await IR spectroscopy of inclusions as well as quantitative measurements of OH absorption bands in feldspar samples to learn whether these quartz inclusions are dry, and are therefore strong, or have hydrous defects that would lead to water weakening.

4.6. Potential Roles of Hydrous Defects and Fluid Inclusions

Water contents within the potassium feldspar starting crystals range from 17 ppm to 4950 ppm (H2O per formula unit feldspar) and the types of hydrous defects vary (Table 2). The driest sample, sanidine contains OH on K sites with concentrations of 17-18ppm (Table 2). The baveno-habit sample contains similar OH defects but in much higher concentrations of 4950 ppm (Table 2). Thus, with the similar plastic strengths exhibited by these two feldspars, the substitution of OH for K in potassium feldspars would seem to have little effect on plastic yielding or flow strength. OH absorption bands of the adularia deformed in this study have been assigned to H2O substituting for K, and it appears to have a concentration of the order of 615 ppm (Table 2). While the strength displayed by this feldspar at T = 900ºC is similar to those of the sanidine and baveno crystals, it is much weaker than the other two potassium feldspars at low temperature (T = 700ºC). These defects might well be compared with molecular water that is

unfreezable in synthetic quartz (Kekulawala et al., 1981), but further experiments are necessary to explore the plastic strength of feldspar crystals with this form of hydrous point defect at varying conditions and defect densities. Water contents of the two microcline starting crystals are large (2380 ppm for PF and 2210 ppm for MF); however, most of this water occurs as fluid inclusions, and I cannot conclude whether mechanisms by which dislocations are affected by fluid inclusions in milky quartz apply to dislocation-fluid inclusion interactions in these potassium feldspars. Irrespective of the different forms of hydrous defects and fluid inclusions in the suite of potassium feldspar single crystals deformed in this study, the dependence of dislocation glide (and possibly climb) on water within the feldspar crystal interior is not as strong as found for quartz single crystals (Kekulawala et al., 1981) or feldspar polycrystalline aggregates (Tullis and Yund, 1980). Water weakening of polycrystalline feldspars may involve grain boundary processes that are facilitated by fluids at grain boundaries (Tullis et al., 1996). Despite differences in plastic flow strength of potassium feldspar starting material that are modest for wide variations in water content, microstructural associations of fluid inclusions and deformation lamellae suggest some interactions of hydrous defects (or water) and dislocation slip. Original fluid inclusions at exsolution lamellae boundaries of the perthitic microcline might serve to nucleate dislocations and accelerate slip where deformation lamellae intersect the fluid inclusions of albite lamellae boundaries (Figure 23). High-resolution IR absorption spectra of samples with these microstructural associations may help to test this inference. Fluid inclusions that decorate deformation lamellae of deformed sanidine (SF-2) may constitute a different interaction between dislocations, hydrous defects, and fluid inclusions (Figure 19). These extremely fine fluid inclusions (~1μm) are not observed in the sanidine starting crystal and they differ from the much larger inclusions of the perthitic microcline. The source of the fluid in these

samples is not clear, given that IR spectra showed only very small concentrations of OH defects and fluid inclusions have not been observed in the thin section prepared from the starting material. However, their occurrence along deformation lamellae suggests that they may have precipitated along dislocations, as documented in water-weakened quartz (McLaren, 1983) following pipe diffusion along mobile dislocations (Bakker and Jansen, 1990).

4.7. Recrystallization

Fine recrystallized feldspar grains (~19 μm in diameter; Figure 22, f) are observed in perthite samples PF-4 and PF-6 deformed in stepping experiments (Figure 22, f), and in white mica sample MF-2 deformed at T=700ºC (Figure 24). The formation of recrystallized grains within these single crystals clearly cannot be explained by any grain boundary processes, leaving only subgrain rotation as a potential mechanism of dynamic recrystallization (Stipp et al., 2010). However, neither subgrains or subgrain walls were detected optically. Instead, recrystallized grains are found at large cleavage fracture surfaces of deformed perthite samples and associated with muscovite inclusions of one of the deformed white microclines. Tullis and Yund (1985) found that cataclastic flow of albite could lead to macroscopically homogeneous deformation and grain size reduction. By similar processes, recrystallized grains at fractures may represent healed, fine-grained products of fracture.

4.8. Thermally Activated Flow Laws

Thermally activated power, experimental, and Peierls resistance flow laws fit the data from the perthite feldspar stepping experiments, and the best flow law is not distinguishable on the basis of fit (Figure 13). The temperature and strain-rate dependencies of differential stress suggest that

crystal plasticity is predominant among deformation mechanisms, since brittle failure by fracture and frictional sliding show only modest dependencies on temperature and strain rate. The absence of optically visible subgrains and very little recrystallization, limited to fractures, suggest that recovery processes during deformation were slow. Thus, mechanical results and deformation microstructures both indicate that dislocation glide is the dominant deformation mechanism, rather than dislocation glide and climb or dislocation creep accommodated by dynamic recrystallization. While the power law between stress and strain rate fits the data well, microstructural observations suggest that feldspar plasticity can be described by either the exponential or Peierls lattice resistance law for dislocation slip. The term α of the exponential glide law is related to an activation area (Poirier, 1985) swept out over several feldspar unit cells by dislocation kinks. Alternatively, the Peierls law may describe dislocation glide with an athermal Peierls stress σ_p value that falls within the range of values determined for glide in other crystalline solids (Kamimura et al., 2013).

Using either flow law, the strain rate-stress relationship of perthitic microcline single crystals is highly nonlinear compared with power laws reported for polycrystalline albite and anorthite deformed by dislocation creep with stress exponents of 3.9 and 3.0, respectively (Shelton and Tullis, 1981; Rybacki and Dresen, 2000). The strain rate-stress laws determined here are in even greater contrast to flow laws of fine-grained anorthite deformed by diffusion creep, with stress exponents n of 1.0 to 2.5 (Wang et al., 1996; Dimanov et al., 1999; Rybacki and Dresen, 2000). The activation enthalpy (H* = 281.7 kJ/mol) determined for slip of perthitic microcline single crystals is comparable to activation enthalpies H* determined for dislocation creep of albite and wet anorthite (234 and 356 kJ/mol, respectively; Shelton, 1981; Rybacki and Dresen, 2000), and much smaller than H* values reported for anorthite diffusion creep, with and without water (H*

= 377 to 585 kJ/mol; Wang et al., 1996; Dimanov et al., 1999; Rybacki and Dresen, 2000).

4.9. Geologic Implications

The microstructures of potassium feldspars deformed in this study compare favorably with feldspar microstructures of naturally deformed granitic rocks at mid-crustal levels and confirm that the same glide mechanisms and mechanical properties apply to continental crustal rocks subject to tectonic stresses and much lower, geologic strain rates. Feldspars of continental lithosphere frequently deform by combined brittle and plastic deformation mechanisms at temperatures of 450^{o} - 580^{o}C, with microstructures consisting of healed microcracks, undulatory extinction and twins, while coexisting quartz deforms by dislocation creep accompanied by dynamic recrystallization (Michibayashi and Masuda, 1993; Mancktelow and Pennacchioni, 2004; Ishii et al., 2007). Mixed brittle and plastic deformation mechanisms continue to high grade conditions of T = 550^{o}C and P = 600-800 MPa in naturally deformed plagioclases (Brander et al., 2012), even while accompanied by dynamic recrystallization. However, at long-term tectonic strain rates plagioclase and alkali feldspars of middle- to deep-level crustal shear zones deform by dislocation and diffusion creep at T = 550^{o} - 850^{o}C, P = 200 - 1800 MPa with little evidence of cracking and relatively low defect densities that are maintained by recovery and dynamic recrystallization (White , 1975; Vidal et al., 1980; Olsen and Kohlstedt, 1984; Kruse and Stünitz, 1999; Rosenberg and Stünitz, 2003; Zavada et al., 2007; Franek et al., 2011). Recrystallization in samples deformed at the experimental strain rate (10^{-6} s^{-1}) of this study is limited to very small volume fractions and evidence of dislocation recovery is limited. Observations of shear zones formed by combined retrograde reactions and shear of layer silicate product phases within granitic host rocks at middle- to shallow crustal levels are also consistent with results of this study, particularly the localized shear observed in white microcline sample

MF-2. Localized shear of secondary micas within this microcline sample demonstrates the importance of weaker layer silicate inclusions within framework silicates to the nucleation of shear zones and subsequent displacement. This is particularly important at low temperature, low pressure conditions of the uppermost crust, for which quartz and feldspars are strong, deforming by cataclasis, and fluid access leads reaction to sericite and other secondary hydrous minerals that are weak (Evans, 1988). The interaction of feldspar deformation and shear of weaker layer silicate inclusions along initially brittle fractures of MF-2 has direct application to understanding the development of fault gouge and phyllonite within quartzofeldspathic rocks (O'Hara, 1988; Hippert, 1998; Bhattacharyya and Mitra, 2011; Farjasovsky et al., 2016).

5. CONCLUSIONS

1. Dislocation glide is the dominant deformation mechanism in potassium feldspars deformed at temperatures of 700º - 900ºC, strain rates of $10^{-6}s^{-1}$ and confining pressures of 1500 MPa. There is no optically detectable evidence of dislocation climb or recovery mechanisms active at these conditions.
2. At the conditions of these experiments, all samples can return to a high symmetry, disordered state. Moreover, exsolved perthitic microcline shows evidence of homogenization to a solid solution alkali feldspar. As a result of the similar symmetry and structural state, all samples exhibit similar mechanical strengths, dislocation glide deformation mechanisms, and consistent temperature dependency despite differences in starting material symmetry and tetrahedral cation order.
3. Brittle-plastic mechanisms are interdependent at the experimental conditions and suggest a significant effect on strength of the lithosphere at similar conditions. The codependency of brittle-plastic mechanisms reduce sample strength more than, if these deformation mechanisms operated independently.
4. Irrespective of different forms of hydrous defects and fluid inclusions in the suite of potassium feldspar single crystals in this study, the dependence of dislocation glide (and possibly climb) on water within the feldspar crystal is not as strong as reported for quartz single crystals or polycrystalline feldspars. Water weakening of polycrystalline feldspars may involve grain boundary processes that are facilitated by interfacial fluids and boundary inclusions.
5. Fluid inclusions in perthitic microcline may facilitate deformation by nucleating dislocations and accelerating slip. Fluid inclusions appear to precipitate along

deformation lamellae, even in dry sanidine samples. Delivery of trace hydrogen defects by pipe diffusion may be facilitated along mobile dislocations, followed by precipitation of fluid inclusions.

6. Brittle-plastic and crystal plastic microstructures developed at T = 700^{o} - 900^{o}C and strain rate = $10^{-6}s^{-1}$ are similar to microstructures of naturally deformed rocks in the lower Amphibolite facies; however, naturally deformed feldspathic rocks tend to exhibit more recrystallization than present in my samples, potentially due to nucleation at grain boundaries facilitated by grain boundary mobility.

REFERENCES

Aines, R. D., Kirby, S. H., Rossman, G. R. J. P., and Minerals, C. o., 1984, Hydrogen speciation in synthetic quartz, v. 11, no. 5, p. 204-212.

Bakker, R. J., and Jansen, J. B. H. J. N., 1990, Preferential water leakage from fluid inclusions by means of mobile dislocations, v. 345, no. 6270, p. 58-60.

Beran, A. J. P., and Minerals, C. o., 1986, A model of water allocation in alkali feldspar, derived from infrared-spectroscopic investigations, v. 13, no. 5, p. 306-310.

Bhattacharyya, K., and Mitra, G. J. J. o. S. G., 2011, Strain softening along the MCT zone from the Sikkim Himalaya: relative roles of quartz and micas, v. 33, no. 6, p. 1105-1121.

Borg, I. Y., and Heard, H. C., Experimental Deformation Of Plagioclases, Berlin, Heidelberg, 1970, Springer Berlin Heidelberg, p. 375-403.

Brace, W., and Kohlstedt, D. J. J. o. G. R. S. E., 1980, Limits on lithospheric stress imposed by laboratory experiments, v. 85, no. B11, p. 6248-6252.

Brady, J. B., and Yund, R. A. J. A. M., 1983, Interdiffusion of K and Na in alkali feldspars; homogenization experiments, v. 68, no. 1-2, p. 106-111.

Brander, L., Svahnberg, H., Piazolo, S. J. C. t. M., and Petrology, 2012, Brittle-plastic deformation in initially dry rocks at fluid-present conditions: transient behaviour of feldspar at mid-crustal levels, v. 163, no. 3, p. 403-425.

Buck, W. R. J. J. o. G. R. S. E., 1991, Modes of continental lithospheric extension, v. 96, no. B12, p. 20161-20178.

Bürgmann, R., and Dresen, G. J. A. R. E. P. S., 2008, Rheology of the lower crust and upper mantle: Evidence from rock mechanics, geodesy, and field observations, v. 36, p. 531-567.

Burov, E., and Watts, A. J. G. t., 2006, The long-term strength of continental lithosphere:" jelly sandwich" or" crème brûlée"?, v. 16, no. 1, p. 4.

Byerlee, J., 1978, Friction of rocks, Rock friction and earthquake prediction, Springer, p. 615-626.

Carlson, D. H., Plummer, C. C., and McGeary, D., 2008, Physical geology: Earth revealed, McGraw-Hill New York.

Chen, S., Hiraga, T., and Kohlstedt, D. L. J. J. o. G. R. S. E., 2006, Water weakening of clinopyroxene in the dislocation creep regime, v. 111, no. B8.

Chester, F. M. J. T., 1988, The brittle-ductile transition in a deformation-mechanism map for halite, v. 154, no. 1-2, p. 125-136.

Chopra, P., and Paterson, M. J. J. o. G. R. S. E., 1984, The role of water in the deformation of dunite, v. 89, no. B9, p. 7861-7876.

Deer, W. A., Howie, R. A., and Zussman, J., 2001, Rock-forming minerals. 4A: Framework silicates. Feldspars, Geological Soc.

Dell'Angelo, L. N., and Tullis, J. J. T., 1996, Textural and mechanical evolution with progressive strain in experimentally deformed aplite, v. 256, no. 1-4, p. 57-82.

Dewey, J. F., and Bird, J. M. J. J. o. g. R., 1970, Mountain belts and the new global tectonics, v. 75, no. 14, p. 2625-2647.

Dieterich, J. H., 1978, Time-dependent friction and the mechanics of stick-slip, Rock friction and earthquake prediction, Springer, p. 790-806.

Dimanov, A., Dresen, G., Xiao, X., and Wirth, R. J. J. o. G. R. S. E., 1999, Grain boundary diffusion creep of synthetic anorthite aggregates: The effect of water, v. 104, no. B5, p. 10483-10497.

Farkašovský, R., Bónová, K., and Košuth, M. J. G., 2016, Microstructural, modal and geochemical changes as a result of granodiorite mylonitisation–a case study from the Rolovská shear zone (Čierna hora Mts, Western Carpathians, Slovakia), v. 22, no. 3, p. 171-190.

Fletcher, C., 2010, Physical Geology: The Science of Earth: The Science of Earth, Wiley Global Education.

Franěk, J., Schulmann, K., Lexa, O., Ulrich, S., Štípská, P., Haloda, J., and Týcová, P. J. J. o. M. G., 2011, Origin of felsic granulite microstructure by heterogeneous decomposition of alkali feldspar and extreme weakening of orogenic lower crust during the Variscan orogeny, v. 29, no. 1, p. 103-130.

Fredrich, J. T., Evans, B., and Wong, T. F. J. J. o. G. R. S. E., 1989, Micromechanics of the brittle to plastic transition in Carrara marble, v. 94, no. B4, p. 4129-4145.

Freed, A. M., Bürgmann, R., Calais, E., Freymueller, J., and Hreinsdóttir, S. J. J. o. G. R. S. E., 2006, Implications of deformation following the 2002 Denali, Alaska, earthquake for postseismic relaxation processes and lithospheric rheology, v. 111, no. B1.

Getsinger, A., Hirth, G., Stünitz, H., and Goergen, E. J. G., Geophysics, Geosystems, 2013, Influence of water on rheology and strain localization in the lower continental crust, v. 14, no. 7, p. 2247-2264.

Griggs, D., 1967, Hydrolytic Weakening of Quartz and Other Silicates*: Geophysical Journal International, v. 14, no. 1-4, p. 19-31.

Griggs, D., and Blacic, J. J. S., 1965, Quartz: anomalous weakness of synthetic crystals, v. 147, no. 3655, p. 292-295.

Hacker, B. R., Kelemen, P. B., Behn, M. D. J. A. R. o. E., and Sciences, P., 2015, Continental lower crust, v. 43, p. 167-205.

Hippertt, J. J. J. o. S. G., 1998, Breakdown of feldspar, volume gain and lateral mass transfer during mylonitization of granitoid in a low metamorphic grade shear zone, v. 20, no. 2-3, p. 175-193.

Hirth, G., and Tullis, J. J. J. o. s. g., 1992, Dislocation creep regimes in quartz aggregates, v. 14, no. 2, p. 145-159.

Holyoke, C. W., Kronenberg, A. K., Newman, J., and Ulrich, C. J. J. o. G. R. S. E., 2014, Rheology of magnesite, v. 119, no. 8, p. 6534-6557.

Holyoke III, C. W., and Kronenberg, A. K. J. T., 2010, Accurate differential stress measurement using the molten salt cell and solid salt assemblies in the Griggs apparatus with applications to strength, piezometers and rheology, v. 494, no. 1-2, p. 17-31.

Houseman, G., and England, P. J. J. o. G. R. S. E., 1986, Finite strain calculations of continental deformation: 1. Method and general results for convergent zones, v. 91, no. B3, p. 3651-3663.

Ishii, K., Kanagawa, K., Shigematsu, N., and Okudaira, T. J. J. o. S. G., 2007, High ductility of K-feldspar and development of granitic banded ultramylonite in the Ryoke metamorphic belt, SW Japan, v. 29, no. 6, p. 1083-1098.

Janecke, S. U., and Evans, J. P. J. G., 1988, Feldspar-influenced rock rheologies, v. 16, no. 12, p. 1064-1067.

Johnson, E. A., and Rossman, G. R. J. A. M., 2003, The concentration and speciation of hydrogen in feldspars using FTIR and 1H MAS NMR spectroscopy, v. 88, no. 5-6, p. 901-911.

Kekulawala, K., Paterson, M., and Boland, J. J. G. M. S., 1981, An experimental study of the role of water in quartz deformation, v. 24, p. 49-60.

Kekulawala, K. R. S. S., Paterson, M., and Boland, J. J. T., 1978, Hydrolytic weakening in quartz, v. 46, no. 1-2, p. T1-T6.

Kerrich, R., Allison, I., Barnett, R. L., Moss, S., Starkey, J. J. C. t. M., and Petrology, 1980, Microstructural and chemical transformations accompanying deformation of granite in a shear zone at Mieville, Switzerland; with implications for stress corrosion cracking and superplastic flow, v. 73, no. 3, p. 221-242.

Kirby, S. H., and McCormick, J. W. J. B. d. M., 1979, Creep hydrolytically weakened synthetic quartz crystals oriented to promote {2-1-10}< 0001> slip: a brief summary of work to date, v. 102, no. 2, p. 124-137.

Kohlstedt, D., Evans, B., and Mackwell, S. J. J. o. G. R. S. E., 1995, Strength of the lithosphere: Constraints imposed by laboratory experiments, v. 100, no. B9, p. 17587-17602.

Kovacs, M., Gandais, M. J. P., and Minerals, C. o., 1980, Transmission electron microscope study of experimentally deformed K-feldspar single crystals, v. 6, no. 1, p. 61-76.

Kronenberg, A. K., Yund, R. A., and Rossman, G. R. J. G. e. C. A., 1996, Stationary and mobile hydrogen defects in potassium feldspar, v. 60, no. 21, p. 4075-4094.

Kronenberg, A. K. J. R. i. M., 1994, Hydrogen speciation and chemical weakening of quartz, v. 29, p. 121-176.

Kruse, R., Stünitz, H., and Kunze, K. J. J. o. S. G., 2001, Dynamic recrystallization processes in plagioclase porphyroclasts, v. 23, no. 11, p. 1781-1802.

Kruse, R., and Stünitz, H. J. T., 1999, Deformation mechanisms and phase distribution in mafic high-temperature mylonites from the Jotun Nappe, southern Norway, v. 303, no. 1-4, p. 223-249.

Kusznir, N., and Park, R. J. G. S., London, Special Publications, 1987, The extensional strength of the continental lithosphere: its dependence on geothermal gradient, and crustal composition and thickness, v. 28, no. 1, p. 35-52.

Le Pichon, X., Francheteau, J., and Bonnin, J., 1973, Developments in Geotectonics: Plate Tectonics, Elsevier Scientific Publishing Company.

Lin, T.-H., Yund, R. J. C. t. M., and Petrology, 1972, Potassium and sodium self-diffusion in alkali feldspar, v. 34, no. 3, p. 177-184.

Linker, M. F., Kirby, S. H., Ord, A., and Christie, J. M. J. J. o. G. R. S. E., 1984, Effects of compression direction on the plasticity and rheology of hydrolytically weakened synthetic quartz crystals at atmospheric pressure, v. 89, no. B6, p. 4241-4255.

Lonka, H., Schulmann, K., and Venera, Z. J. J. o. S. G., 1998, Ductile deformation of tonalite in the Suomusjärvi shear zone, south-western Finland, v. 20, no. 6, p. 783-798.

Mancktelow, N. S., and Pennacchioni, G. J. J. o. S. G., 2004, The influence of grain boundary fluids on the microstructure of quartz-feldspar mylonites, v. 26, no. 1, p. 47-69.

Marshall, D., McLaren, A. J. P., and minerals, c. o., 1977, Deformation mechanisms in experimentally deformed plagioclase feldspars, v. 1, no. 4, p. 351-370.

Masuda, K., Arai, T., Takahashi, M. J. P. i. E., and Science, P., 2019, Effects of frictional properties of quartz and feldspar in the crust on the depth extent of the seismogenic zone, v. 6, no. 1, p. 1-8.

McLaren, A., Cook, R., Hyde, S., Tobin, R. J. P., and Minerals, C. o., 1983, The mechanisms of the formation and growth of water bubbles and associated dislocation loops in synthetic quartz, v. 9, no. 2, p. 79-94.

Mei, S., and Kohlstedt, D. L. J. J. o. G. R. S. E., 2000, Influence of water on plastic deformation of olivine aggregates: 1. Diffusion creep regime, v. 105, no. B9, p. 21457-21469.

Miranda, E. A., Hirth, G., and John, B. E. J. J. o. S. G., 2016, Microstructural evidence for the transition from dislocation creep to dislocation-accommodated grain boundary sliding in naturally deformed plagioclase, v. 92, p. 30-45.

Mosenfelder, J. L., Rossman, G. R., and Johnson, E. A. J. A. M., 2015, Hydrous species in feldspars: A reassessment based on FTIR and SIMS, v. 100, no. 5-6, p. 1209-1221.

Mukai, H., Austrheim, H., Putnis, C. V., and Putnis, A. J. J. o. P., 2014, Textural evolution of plagioclase feldspar across a shear zone: implications for deformation mechanism and rock strength, v. 55, no. 8, p. 1457-1477.

Negrini, M., Stünitz, H., Nasipuri, P., Menegon, L., and Morales, L. F. J. J. o. G. R. S. E., 2014, Semibrittle deformation and partial melting of perthitic K-feldspar: An experimental study, v. 119, no. 4, p. 3478-3502.

O'Hara, K. J. T., 1988, Fluid flow and volume loss during mylonitization: an origin for phyllonite in an overthrust setting, North Carolina USA, v. 156, no. 1-2, p. 21-36.

Olsen, T. S., Kohlstedt, D. L. J. P., and Minerals, C. o., 1984, Analysis of dislocations in some naturally deformed plagioclase feldspars, v. 11, no. 4, p. 153-160.

Pearce, M. A., Wheeler, J., and Prior, D. J. J. J. o. S. G., 2011, Relative strength of mafic and felsic rocks during amphibolite facies metamorphism and deformation, v. 33, no. 4, p. 662-675.

Rosenberg, C. L., and Stünitz, H. J. J. o. S. G., 2003, Deformation and recrystallization of plagioclase along a temperature gradient: an example from the Bergell tonalite, v. 25, no. 3, p. 389-408.

Rudnick, R. L., and Fountain, D. M. J. R. o. g., 1995, Nature and composition of the continental crust: a lower crustal perspective, v. 33, no. 3, p. 267-309.

Rybacki, E., and Dresen, G. J. J. o. G. R. S. E., 2000, Dislocation and diffusion creep of synthetic anorthite aggregates, v. 105, no. B11, p. 26017-26036.

Rybacki, E., Wirth, R., and Dresen, G. J. J. o. G. R. S. E., 2010, Superplasticity and ductile fracture of synthetic feldspar deformed to large strain, v. 115, no. B8.

Scandale, E., Gandais, M., Willaime, C. J. P., and Minerals, C. o., 1983, Transmission electron microscopic study of experimentally deformed K-feldspar single crystals, v. 9, no. 3-4, p. 182-187.

Scholz, C. H. J. A. R. o. E., and Sciences, P., 1989, Mechanics of faulting, v. 17, no. 1, p. 309-334.

Scruggs, V., and Tullis, T. J. T., 1998, Correlation between velocity dependence of friction and strain localization in large displacement experiments on feldspar, muscovite and biotite gouge, v. 295, no. 1-2, p. 15-40.

Seaman, S., Williams, M., Jercinovic, M., Koteas, G., and Brown, L. J. G., 2013, Water in nominally anhydrous minerals: Implications for partial melting and strain localization in the lower crust, v. 41, no. 10, p. 1051-1054.

Shelton, G., and Tullis, J., 1981, Experimental flow laws for crustal rocks, Volume 62: EOS Trans. , AGU.

Shigematsu, N., and Tanaka, H. J. J. o. S. G., 2000, Dislocation creep of fine-grained recrystallized plagioclase under low-temperature conditions, v. 22, no. 1, p. 65-79.

Sibson, R. H. J. J. o. t. G. S., 1983, Continental fault structure and the shallow earthquake source, v. 140, no. 5, p. 741-767.

Sibson, R. J. J. o. t. G. S., 1977, Fault rocks and fault mechanisms, v. 133, no. 3, p. 191-213.

Smith, J. V., and Brown, W. L., 1988, Feldspar Minerals: Crystal Structures, Physical, Chemical, and Microtextural Properties, Springer-Verlag.

Starkey, J., Glide twinning in the plagioclase feldspars, in Proceedings Metall. Soc. Conf1964, Volume 25, p. 177-191.

Stipp, M., Tullis, J., Scherwath, M., and Behrmann, J. H. J. G., 2010, A new perspective on paleopiezometry: Dynamically recrystallized grain size distributions indicate mechanism changes, v. 38, no. 8, p. 759-762.

Stünitz, H., Gerald, J. F., and Tullis, J. J. T., 2003, Dislocation generation, slip systems, and dynamic recrystallization in experimentally deformed plagioclase single crystals, v. 372, no. 3-4, p. 215-233.

Stünitz, H., Thust, A., Heilbronner, R., Behrens, H., Kilian, R., Tarantola, A., and Fitz Gerald, J. J. J. o. G. R. S. E., 2017, Water redistribution in experimentally deformed natural milky quartz single crystals—Implications for H2O-weakening processes, v. 122, no. 2, p. 866-894.

Tielke, J., Mecklenburgh, J., Mariani, E., and Wheeler, J. J. J. o. G. R. S. E., 2019, The influence of water on the strength of olivine dislocation slip systems, v. 124, no. 7, p. 6542-6559.

Tullis, J., and Yund, R. A. J. G., 1985, Dynamic recrystallization of feldspar: A mechanism for ductile shear zone formation, v. 13, no. 4, p. 238-241.

Tullis, J., and Yund, R. A. J. G., 1987, Transition from cataclastic flow to dislocation creep of feldspar: Mechanisms and microstructures, v. 15, no. 7, p. 606-609.

Tullis, J., and Yund, R. A. J. J. o. G. R., 1977, Experimental deformation of dry Westerly granite, v. 82, no. 36, p. 5705-5718.

Tullis, J., and Yund, R. A. J. J. o. S. G., 1980, Hydrolytic weakening of experimentally deformed Westerly granite and Hale albite rock, v. 2, no. 4, p. 439-451.

Tullis, J., and Yund, R. A. J. J. o. S. G., 1991, Diffusion creep in feldspar aggregates: experimental evidence, v. 13, no. 9, p. 987-1000.

Turcotte, D., Liu, J., and Kulhawy, F. J. J. o. G. R. S. E., 1984, The role of an intracrustal asthenosphere on the behavior of major strike-slip faults, v. 89, no. B7, p. 5801-5816.

van der Werf, T., Chatzaras, V., Kriegsman, L. M., Kronenberg, A., Tikoff, B., and Drury, M. R. J. S. E., 2017, Constraints on the rheology of lower crust in a strike-slip plate boundary: Evidence from the San Quintin xenoliths, Baja California, Mexico, v. 8, no. 6, p. 1211-1239.

Vidal, J.-L., Kubin, L., Debat, P., and Soula, J.-C. J. L., 1980, Deformation and dynamic recrystallization of K feldspar augen in orthogneiss from Montagne Noire, Occitania, southern France, v. 13, no. 3, p. 247-255.

Wang, Z., Dresen, G., and Wirth, R. J. G. r. l., 1996, Diffusion creep of fine-grained polycrystalline anorthite at high temperature, v. 23, no. 22, p. 3111-3114.

White, S. J. C. t. M., and Petrology, 1975, Tectonic deformation and recrystallisation of oligoclase, v. 50, no. 4, p. 287-304.

Willaime, C., Christie, J., and Kovacs, M.-P. J. B. d. M., 1979, Experimental deformation of K-feldspar single crystals, v. 102, no. 2, p. 168-177.

Willaime, C., and Gandais, M. J. B. d. M., 1977, Electron microscope study of plastic defects in experimentally deformed alkali feldspars, v. 100, no. 5, p. 263-271.

Woensdregt, C. F. J. F. D., 1993, Hartman–Perdok theory: influence of crystal structure and crystalline interface on crystal growth, v. 95, p. 97-107.

Woensdregt, C. J. Z. f. K.-C. M., 1982, Crystal morphology of monoclinic potassium feldspars: A qualitative approach with special emphasis on the Periodic Bond Chain Theory of Hartman and Perdok, v. 161, no. 1-2, p. 15-33.

Závada, P., Schulmann, K., Konopásek, J., Ulrich, S., and Lexa, O. J. J. o. G. R. S. E., 2007, Extreme ductility of feldspar aggregates—Melt-enhanced grain boundary sliding and creep failure: Rheological implications for felsic lower crust, v. 112, no. B10.

Zhang, M., Salje, E., Carpenter, M., Parsons, I., Kroll, H., Reed, S., and Graeme-Barber, A. J. A. M., 1997, Exsolution and Al-Si disorder in alkali feldspars: Their analysis by infrared spectroscopy, v. 82, no. 9-10, p. 849-857.

Zhang, M., Wruck, B., Barber, A. G., Salje, E., and Carpenter, M. J. A. M., 1996, Phonon spectra of alkali feldspars: phase transitions and solid solutions, v. 81, no. 1-2, p. 92-104.

Zhong, S. J. J. o. G. R. S. E., 1997, Dynamics of crustal compensation and its influences on crustal isostasy, v. 102, no. B7, p. 15287-15299.

APPENDIX A FIGURES

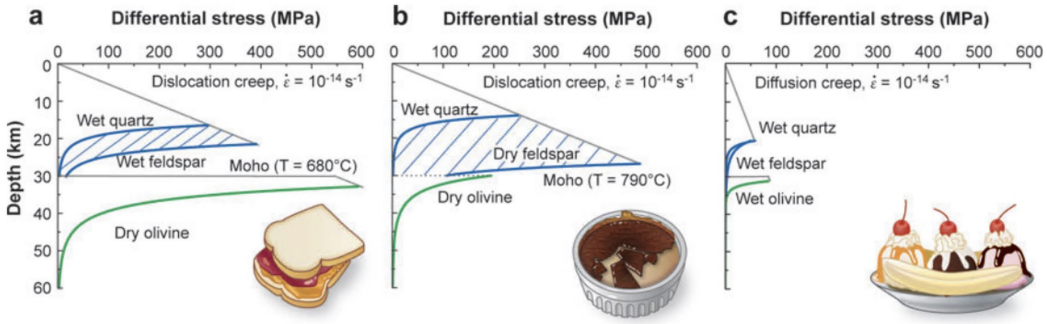

Figure 1. Continental lithosphere models. Plotting differential stress for deformation at a constant strain rate as a function of depth. **(a)** The jelly sandwich model of lithosphere, representing strong upper crust and upper mantle with a low strength lower crust (directly above the Moho), due to wet quartz and feldspar flow. Flow laws of olivine predict a transition in the upper mantle to asthenosphere where deformation proceeds at negligible stresses. **(b)** The crème brûlée model of continental lithosphere consists of high strength silicates, including frictional strengths of quartz at shallow depths, strong dry feldspars of the lower crust, and strong upper mantle governed by olivine deformation, until olivine creep strengths are decreased at increased temperatures at depth. **(c)** The banana split model representing a consistently weak lithosphere at a plate boundary, made up of weak silicates deforming in the presence of water. Reprinted from (Bürgmann and Dresen, 2008)

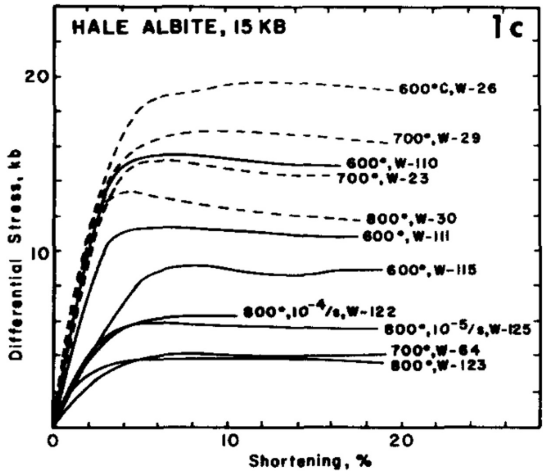

Figure 2. Stress - shortening strain results for polycrystalline Hale albite at varying temperatures and strain rates at high confining pressures (1000-1500 MPa). Stress-strain results for samples designated as 'wet' (with 0.2 wt % added water), shown as solid lines, exhibit flow strengths about half the flow stresses measured for 'dry' samples (dried at 160°C), with stress-strain curves shown as dashed lines. Reprinted from (Tullis and Yund, 1980)

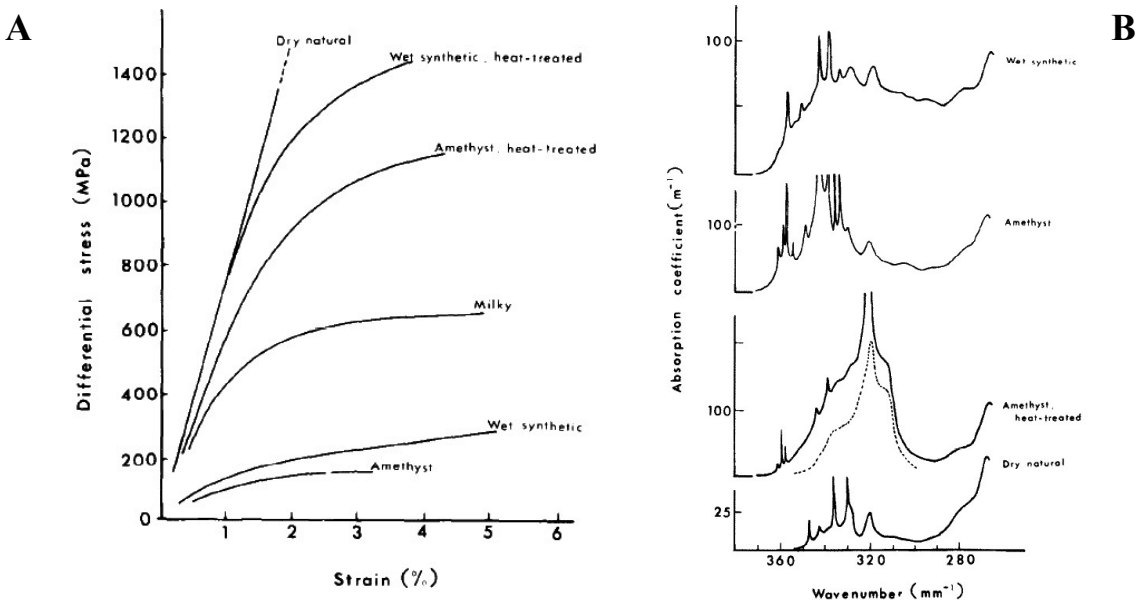

Figure 3. Water weakening of quartz single crystals. A. Stress-strain data for natural and synthetic, amethyst and milky quartz crystals. B. Corresponding IR absorption spectra of natural and synthetic quartz crystals showing broad OH absorptions due to molecular water clusters and sharp OH absorption bands due to hydrogen defects (measured at 4 K). Reprinted from (Kekulawala et al., 1978).

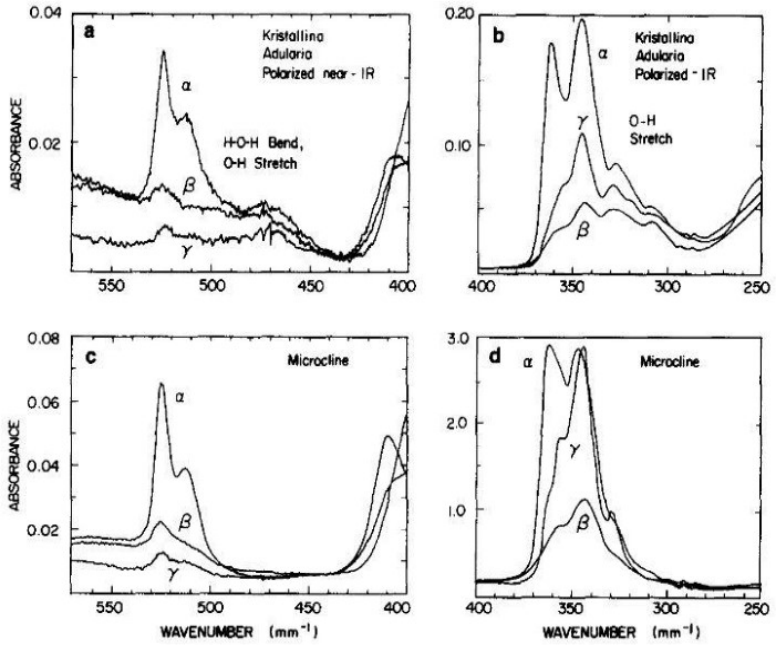

Figure 4. Comparisons of infrared (IR) and near infrared spectra of adularia and microcline feldspars. (a) Adularia near-IR (b) Adularia IR (c) Microcline near-IR (d) Microcline IR. Reprinted from (Kronenberg et al., 1996)

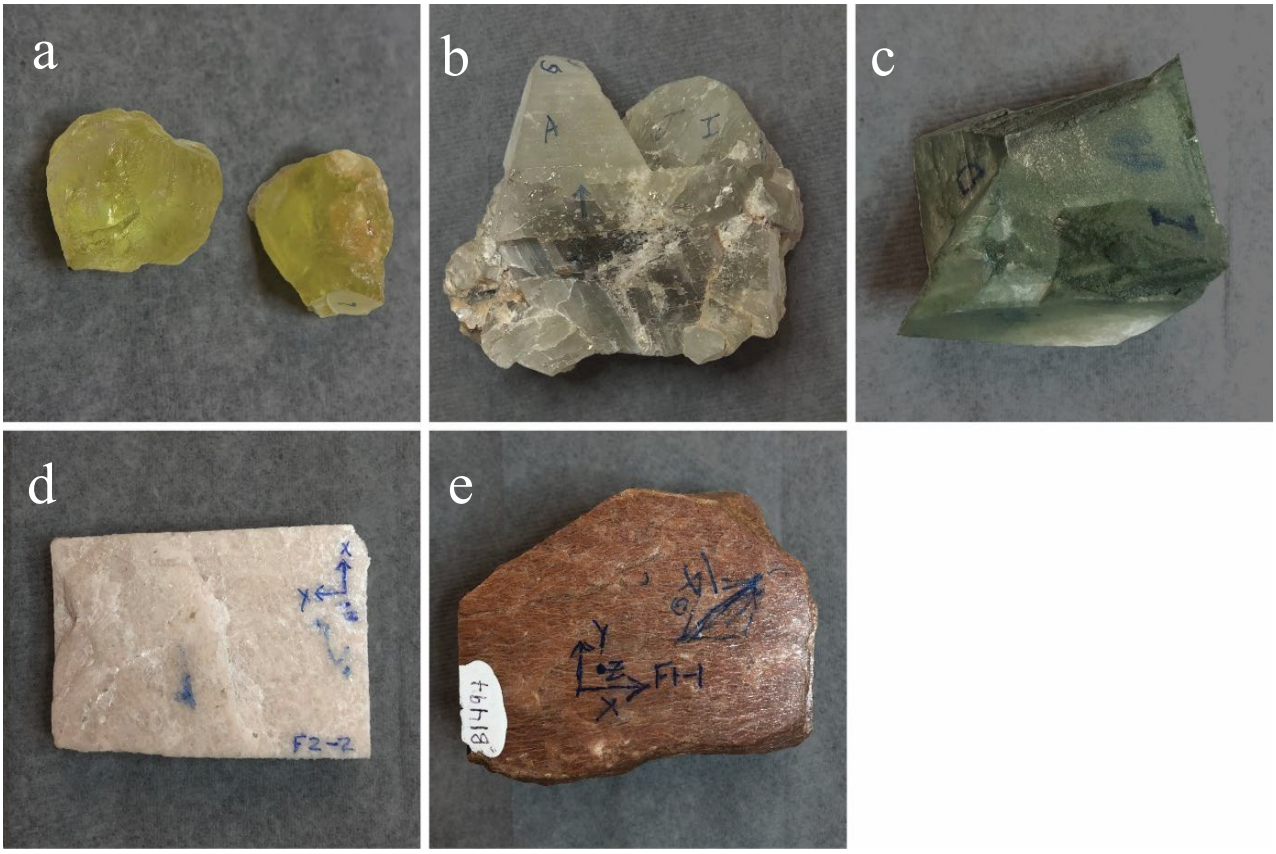

Figure 5. Potassium feldspar crystals with starting material ID, and source location:

(a) Sanidine, SFP1 and SFP2 (SF) Pakistan

(b) Baveno, BF, Norway

(c) Adularia, AF, Alps

(d) White Microcline, MF, location unknown

(e) Red perthitic Microcline, PF, Petrick Quarry, Texas

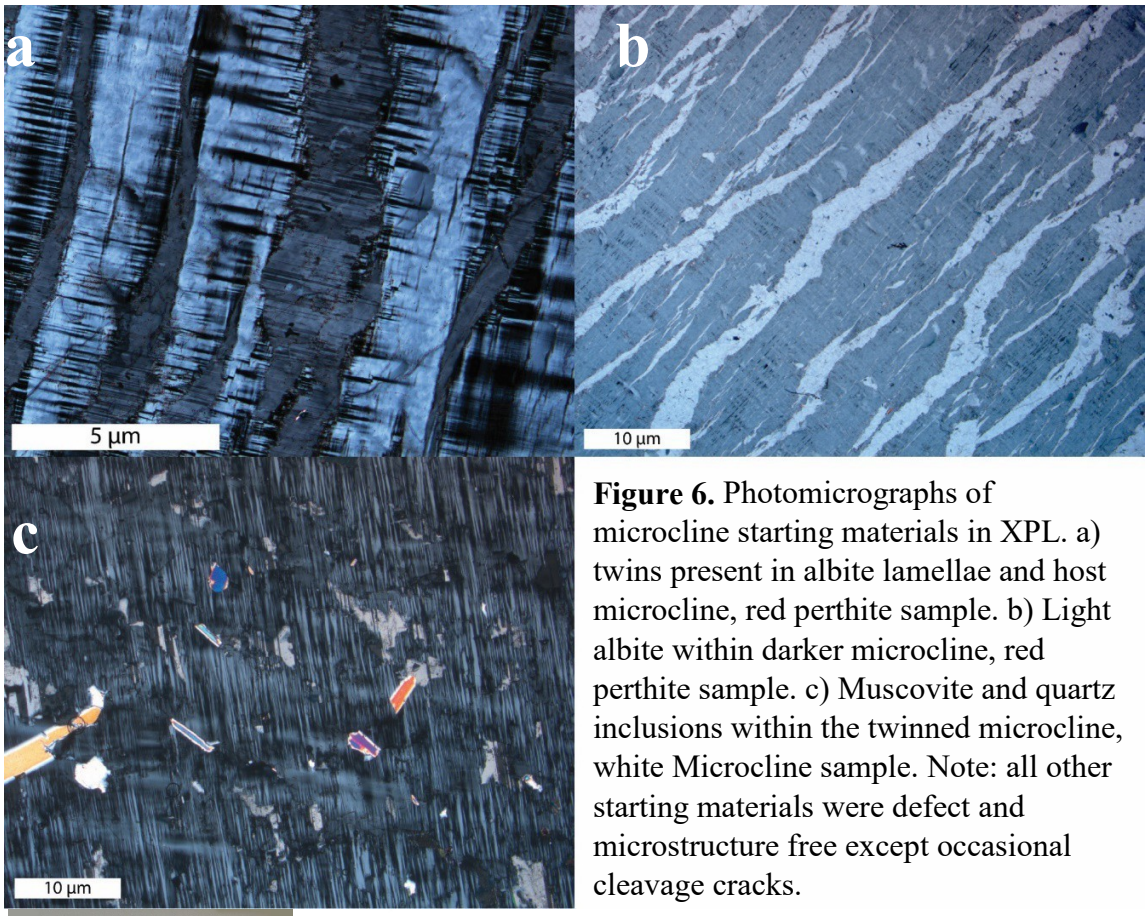

Figure 6. Photomicrographs of microcline starting materials in XPL. a) twins present in albite lamellae and host microcline, red perthite sample. b) Light albite within darker microcline, red perthite sample. c) Muscovite and quartz inclusions within the twinned microcline, white Microcline sample. Note: all other starting materials were defect and microstructure free except occasional cleavage cracks.

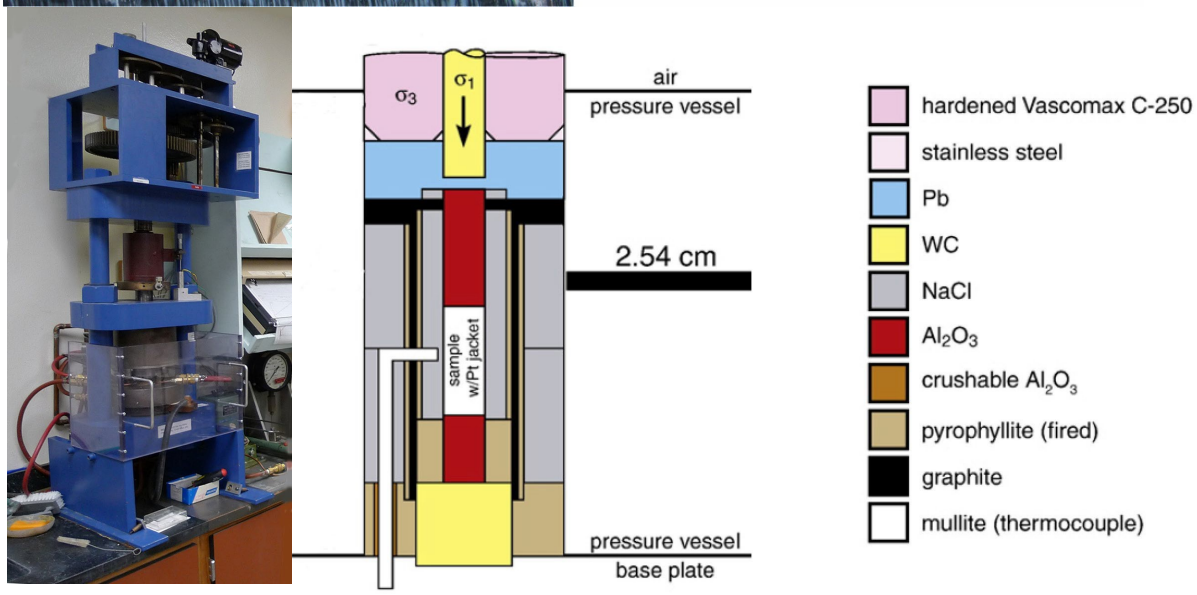

Figure 7. Griggs triaxial deformation apparatus. (a) High pressure and temperature are enables in the Griggs solid-medium piston-cylinder apparatus (b) by using a weak solid-salt assembly, which approximates a high isostatic pressure.

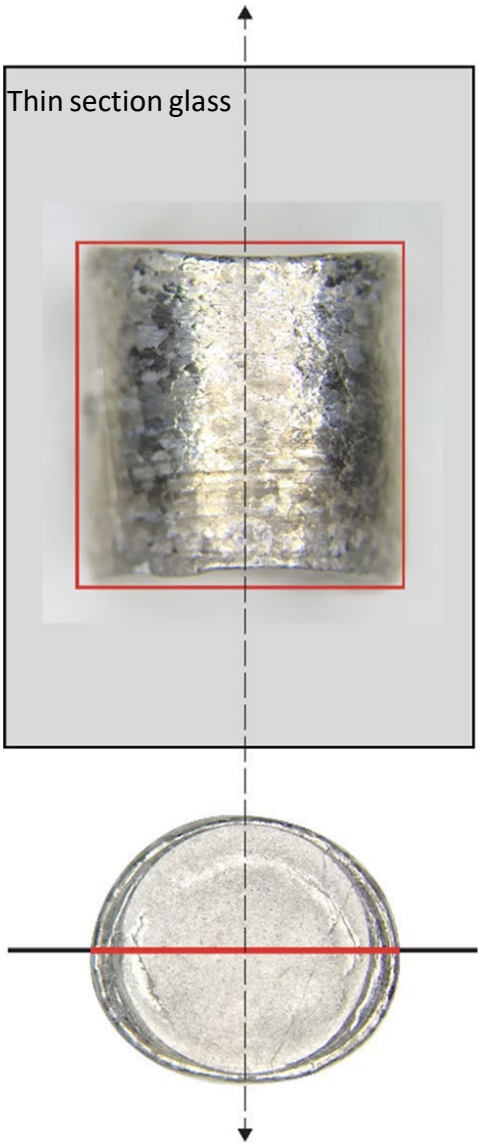

Figure 8. Images of deformed sample PF-4. Within its metal jacket with orientation of thin section shown schematically in both views. Cylindrical samples deformed by way of the two principal slip systems lead to shortened elliptical cylinders with the slip directions projected on the samples long elliptical axis.

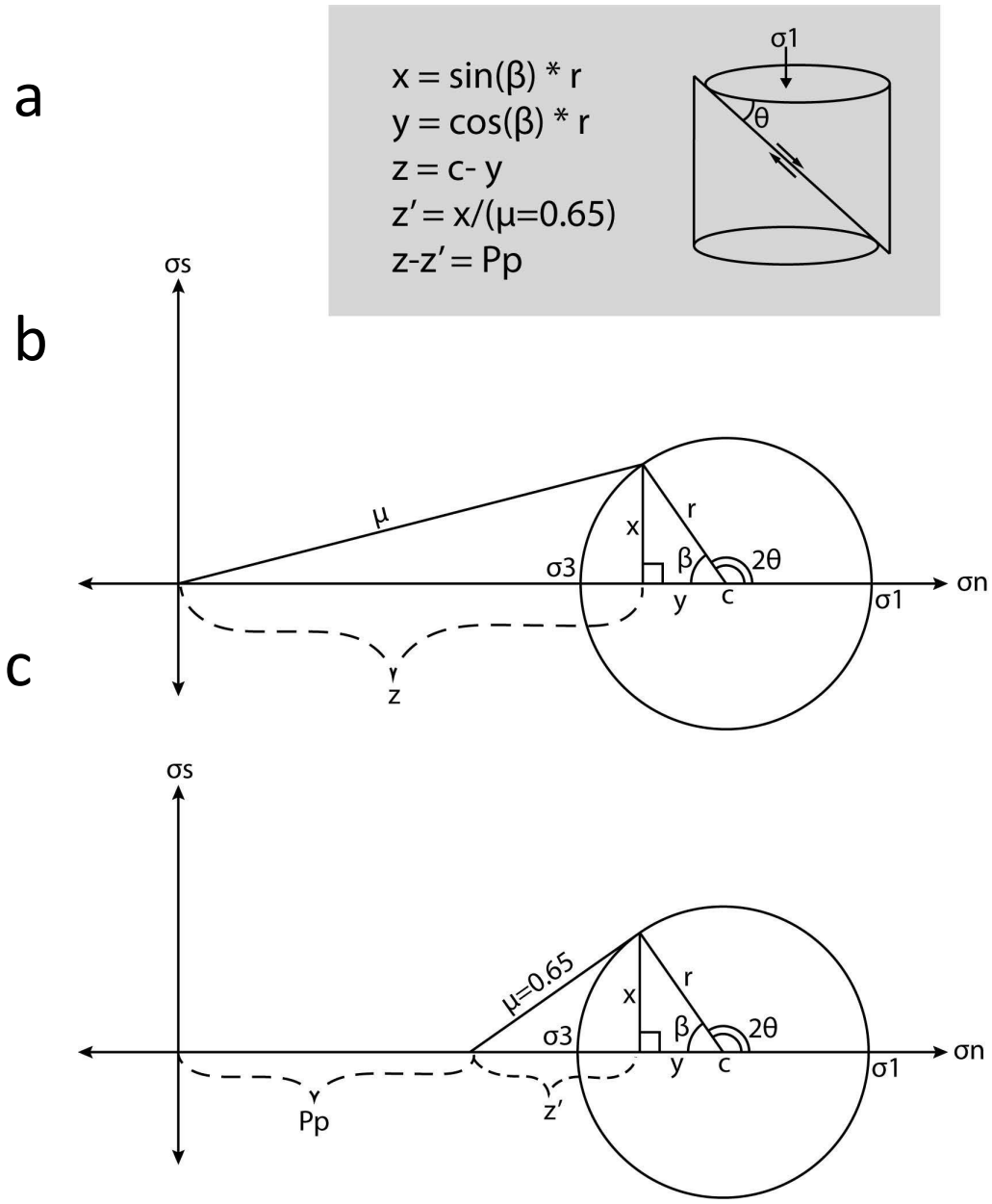

Figure 9. Mohr circle construction used to evaluate frictional failure conditions for deformed simgle crystals that exhibit sample-scale cleavage fractures. (a) Variables and equations listed in dark gray box along with representative sample schematic showing fracture orientation. (b) Mohr circle constructed for pore pressure, Pp = 0. The friction coefficient, μ, is determined for each sample with a sample-scale fracture using the fracture angle and experimental stress state. (c) Mohr circle constructed for high Pp (> 0 MPa) and an assumed friction coefficient for feldspar surfaces (μ = 0.65) to find the minimum Pp required for failure.

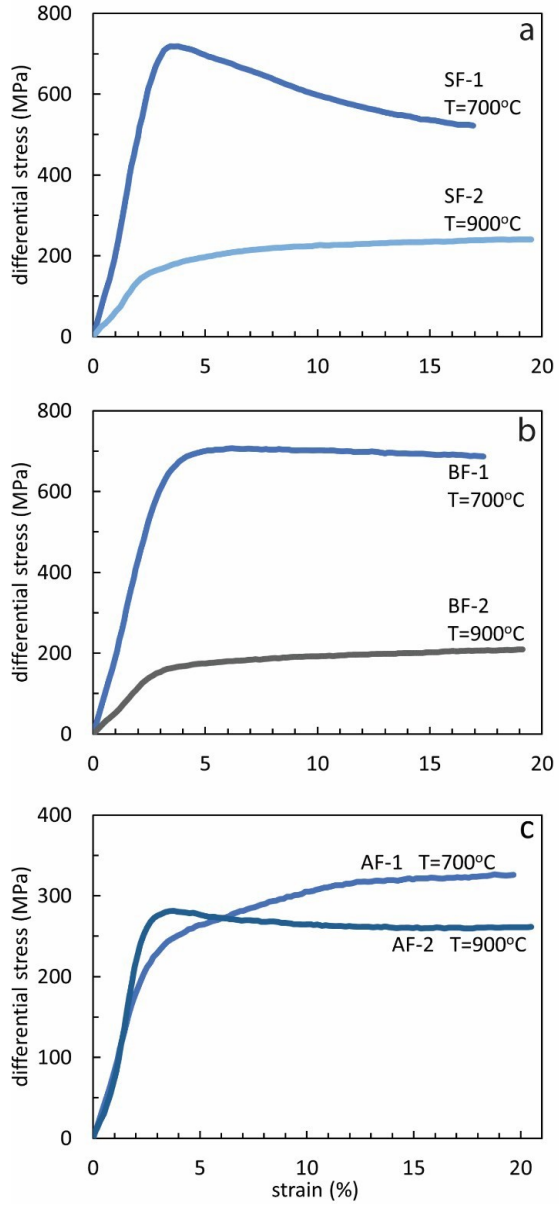

axial

Figure 10. Compressive differential stress (σ1-σ3)(MPa) vs. axial strain (%) of feldspar crystals deformed at Pc=1500MPa and strain rate =1.7*$10^{-6}s^{-1}$. (a) Sanidine (SF) single crystals cored in [001] direction. Samples are from two different single crystals with similar water content and composition. (b) Baveno-habit (BF) deformed in the [012] direction.
(c) Adularia (AF) samples deformed in the [012] direction

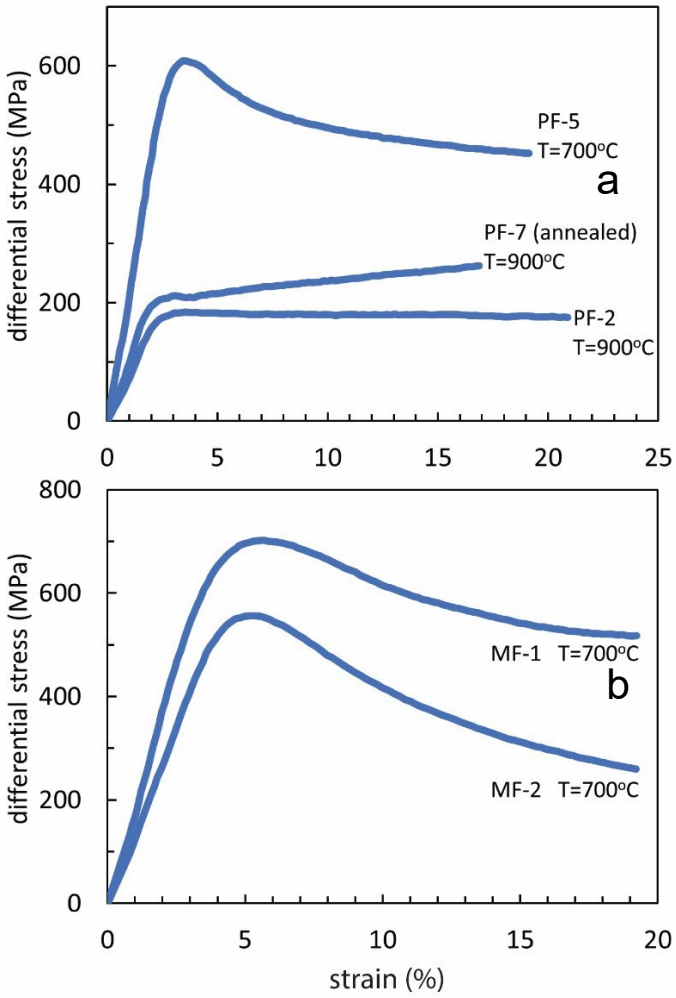

Figure 11. Compressive differential stress (MPa) vs strain (%) plots. (a) red perthitic microcline, PF and (b) white microcline, MF samples deformed in [012] direction at Pc=1500MPa, T=700, 900ₒC and strain rate=1.6-2.0*$10^{-6}S^{-1}$, .

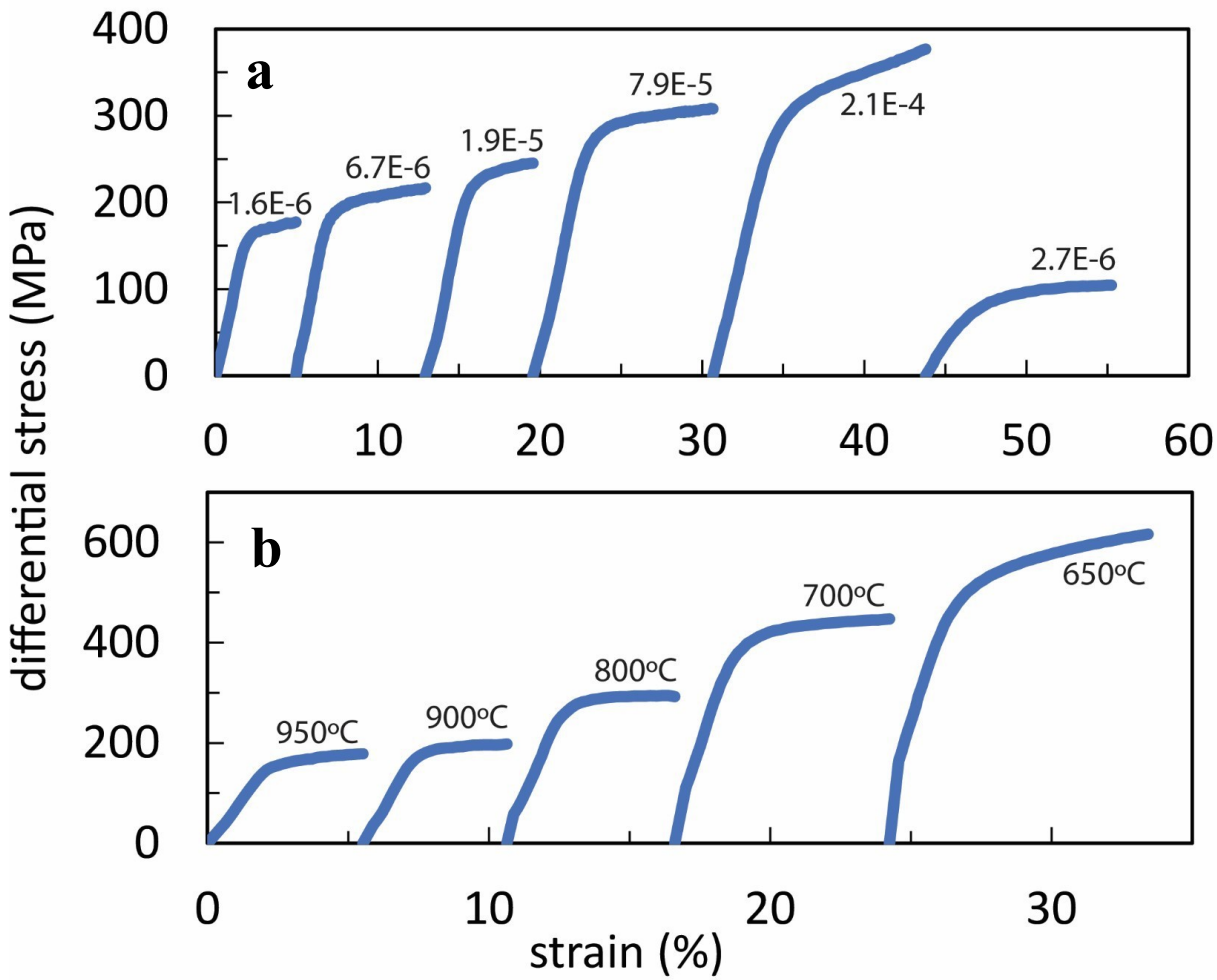

Figure 12. Differential stress (MPa) and strain (%) plots for stepping experiments PF-6 and PF-4. Both experiments were conducted at Pc=1500MPa on red perthitic microcline. a) PF-6 strain rate-stepping experiment performed at T = 900ºC, with strain rates labeled for corresponding curves. (b) PF-4 Temperature-stepping experiment performed at $\dot{\varepsilon}$ =~$1.65*10^{-6}s^{-1}$, with sequential decreases in temperature leading to increasing differential stresses. Temperatures are labeled for corresponding curves.

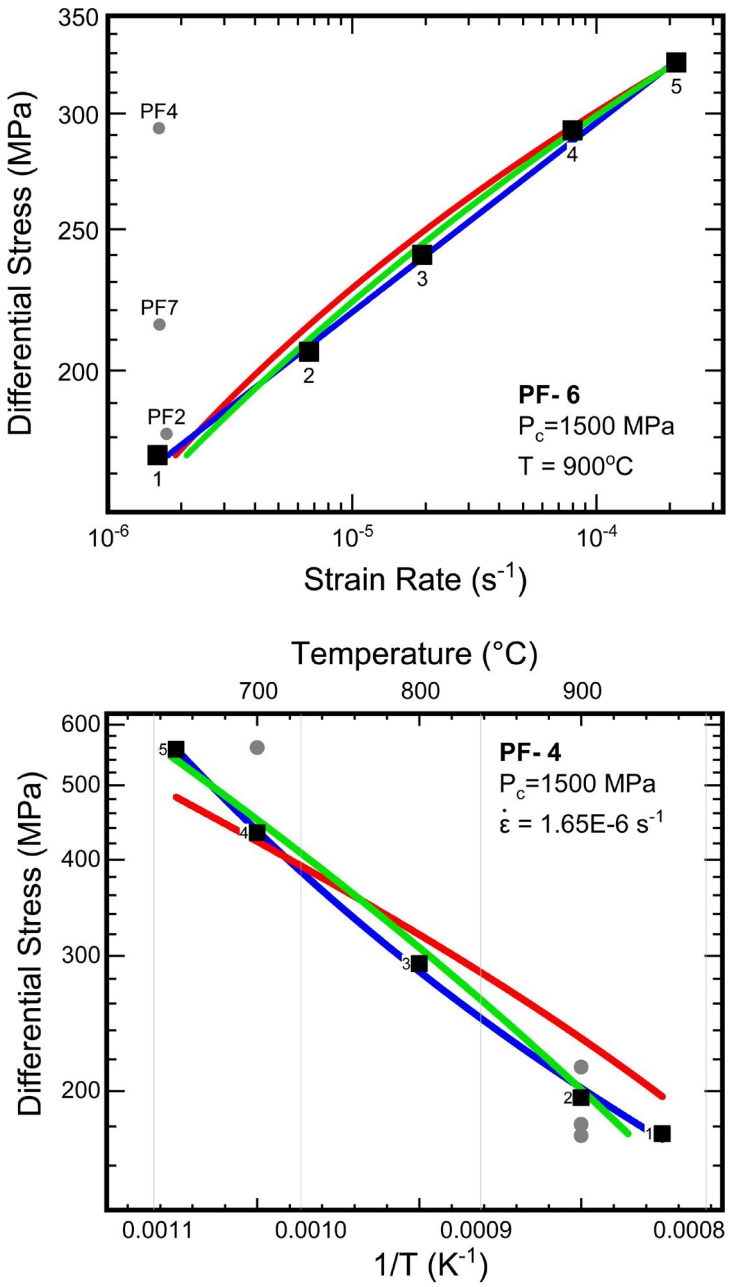

Figure 13. Data for PF-6 and PF-4 plotted as black squares and labeled in step order, single condition experiments plotted as gray circles to show global fit. The best fit of the power law (blue), exponential glide law (red) and Peierls lattice resistance law (green) are shown. (a) Dependence of red perthitic microcline strength on strain rate, in terms of log(differential stress) vs log(strain rate). Note: the 6th PF6 step plots below the curve and was not used in best-fit analysis. (b) Strength of red perthitic microcline as a function of temperature, shown as log(differential stress) vs 1/T as absolute temperature.

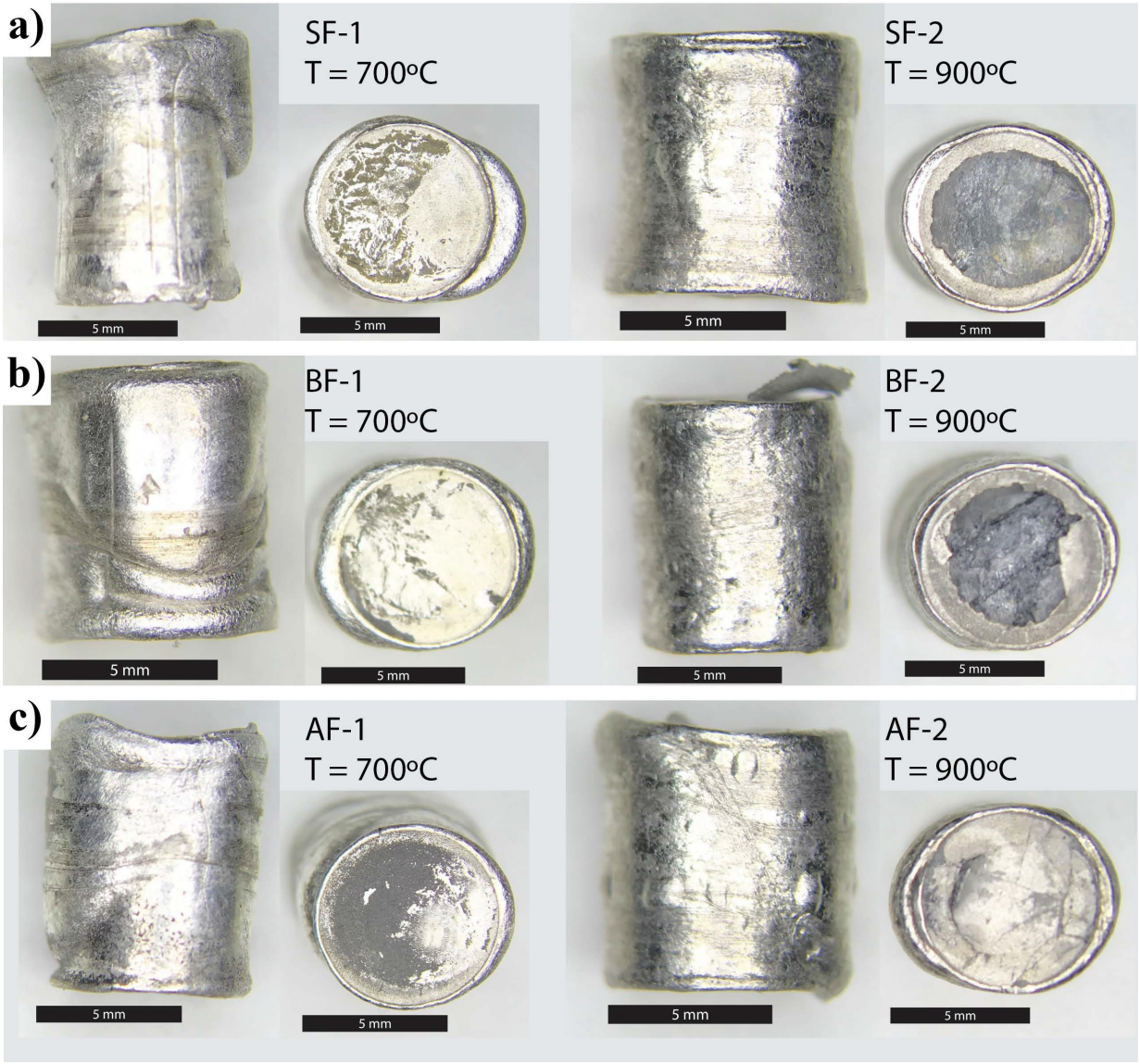

Figure 14. Reflected light micrographs of deformed sanidine, baveno, and adularia cores in the jacket - taken before thin section preparation. Low temperature (T=700ºC) samples are jacketed in Ag foil and Ag jackets with a Ag disk at core ends. High temperature samples are jacketed in a thick Ni sleeve and Pt jacket with both Ni and Pt disks at the core ends.
a) Sanidine samples SF-1 and SF-2 b) Baveno samples BF-1 and BF-2 c) Adularia samples AF-1 and AF-2

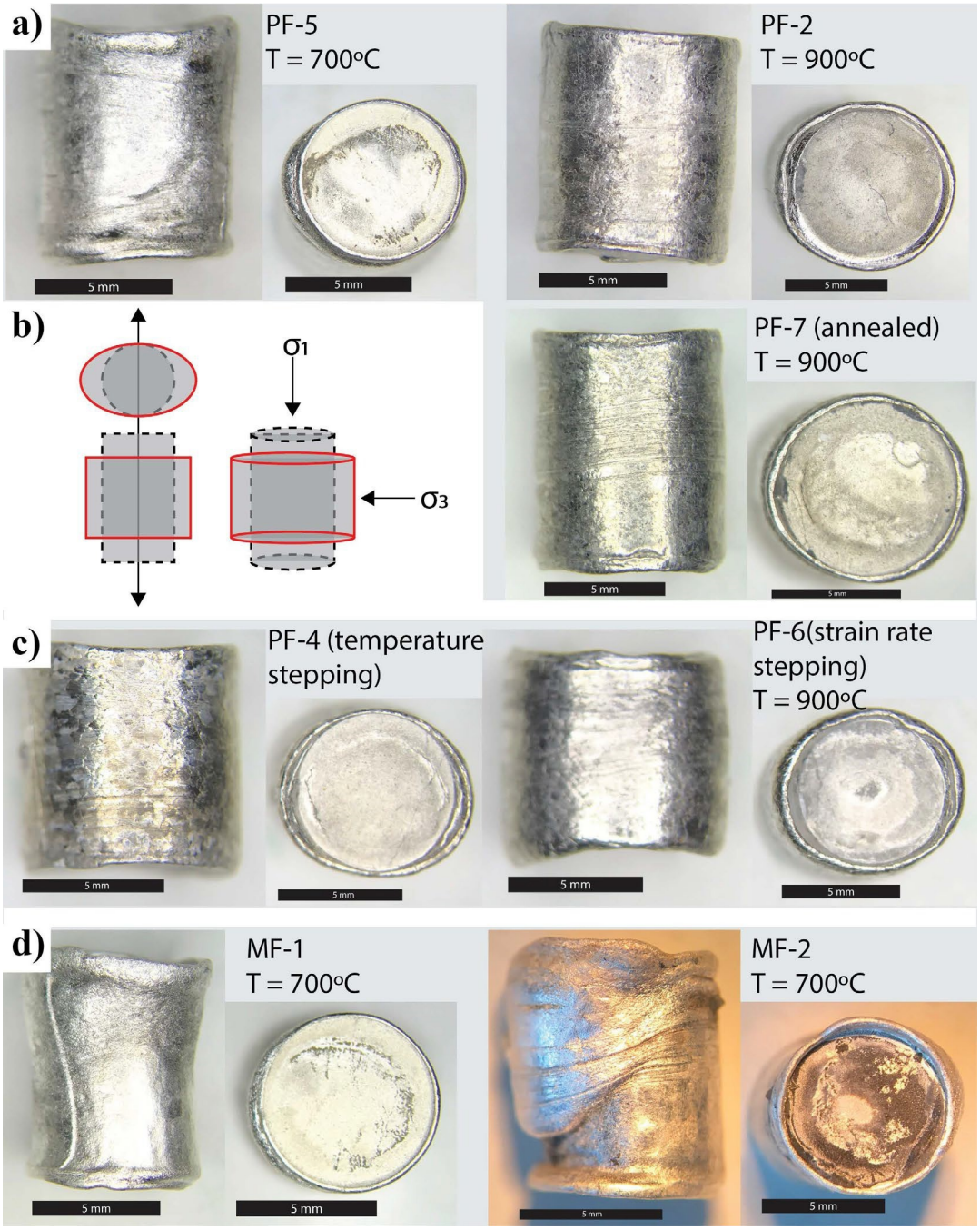

Figure 15. Reflected light micrographs of deformed red perthite and white microcline cores in the jacket - taken before thin section preparation. Low temperature (T=700°C) samples are jacketed in Ag foil and Ag jacket with a Ag disk at core ends. High temperature samples are jacketed in a thick Ni jacket and Pt jacket with both Ni and Pt disks at the core ends. a) red perthite samples, PF-5, PF-3, PF-7 b) idealized schematic of core before deformation (dashed outline) and after deformation (red line) assuming volume remains constant. c) condition stepping experiments on red perthite, PF-4 and PF-6. d) deformed white microcline samples, MF-1 and MF-2.

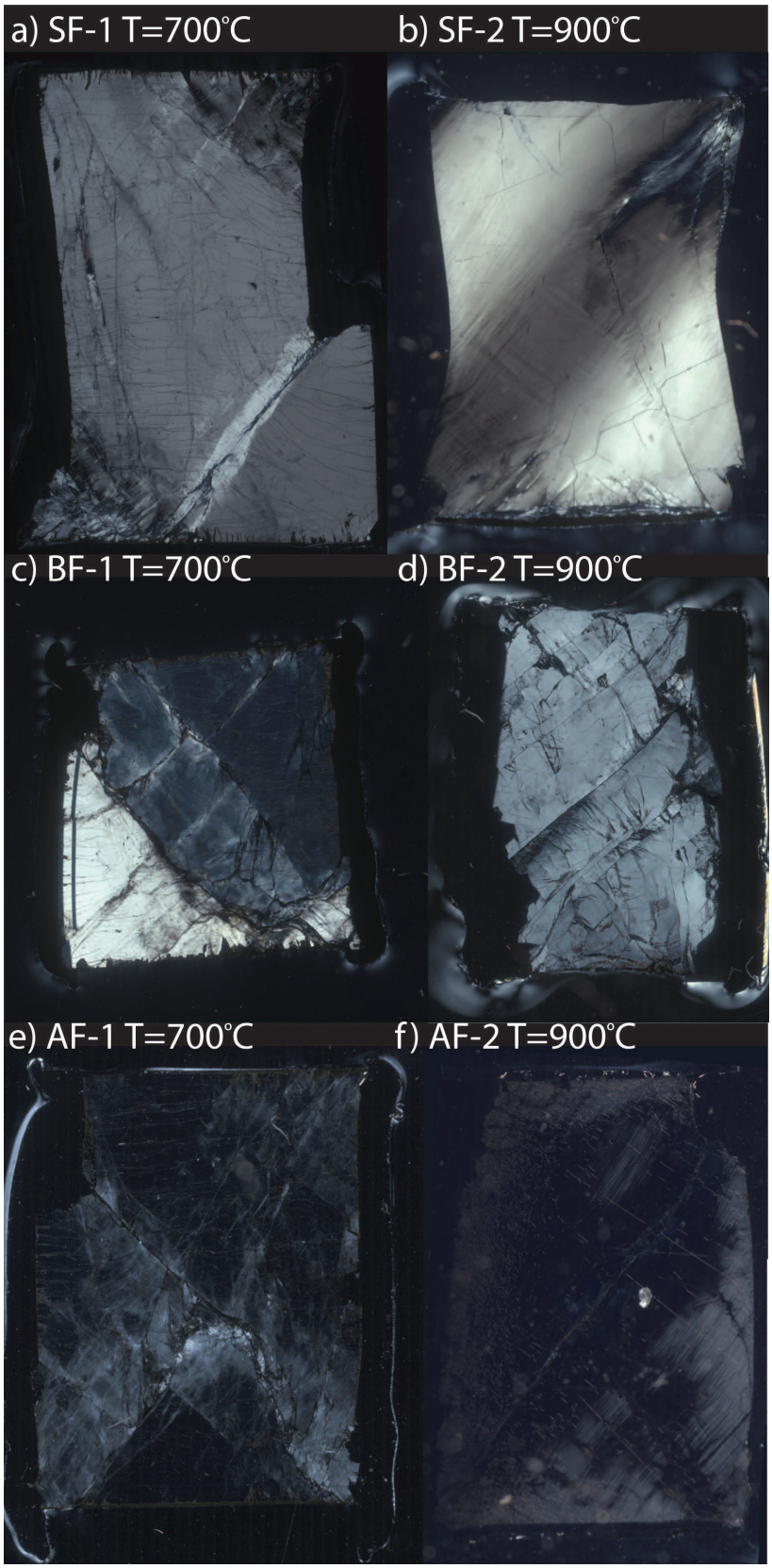

Figure 16. Full sample XPL photomicrographs are shown for deformed sanidine, baveno, and adularia samples. a) SF-1contains ubiquitous microcracks and a large cleavage fracture. b) SF-2 contains a broad deformation band marked by undulatory extinction with perpendicular linear bands of undulatory extinction. c) BF-1 bicrystal with different orientations highlighted by difference in birefringence. d) BF-2 contains cleavage fractures throughout the deformed core. e) AF-1 contains large fractures, correlated microcracking and undulatory extinction localized in heavily fractured areas. f) AF2 sample contains parallel fractures and mechanical twins.

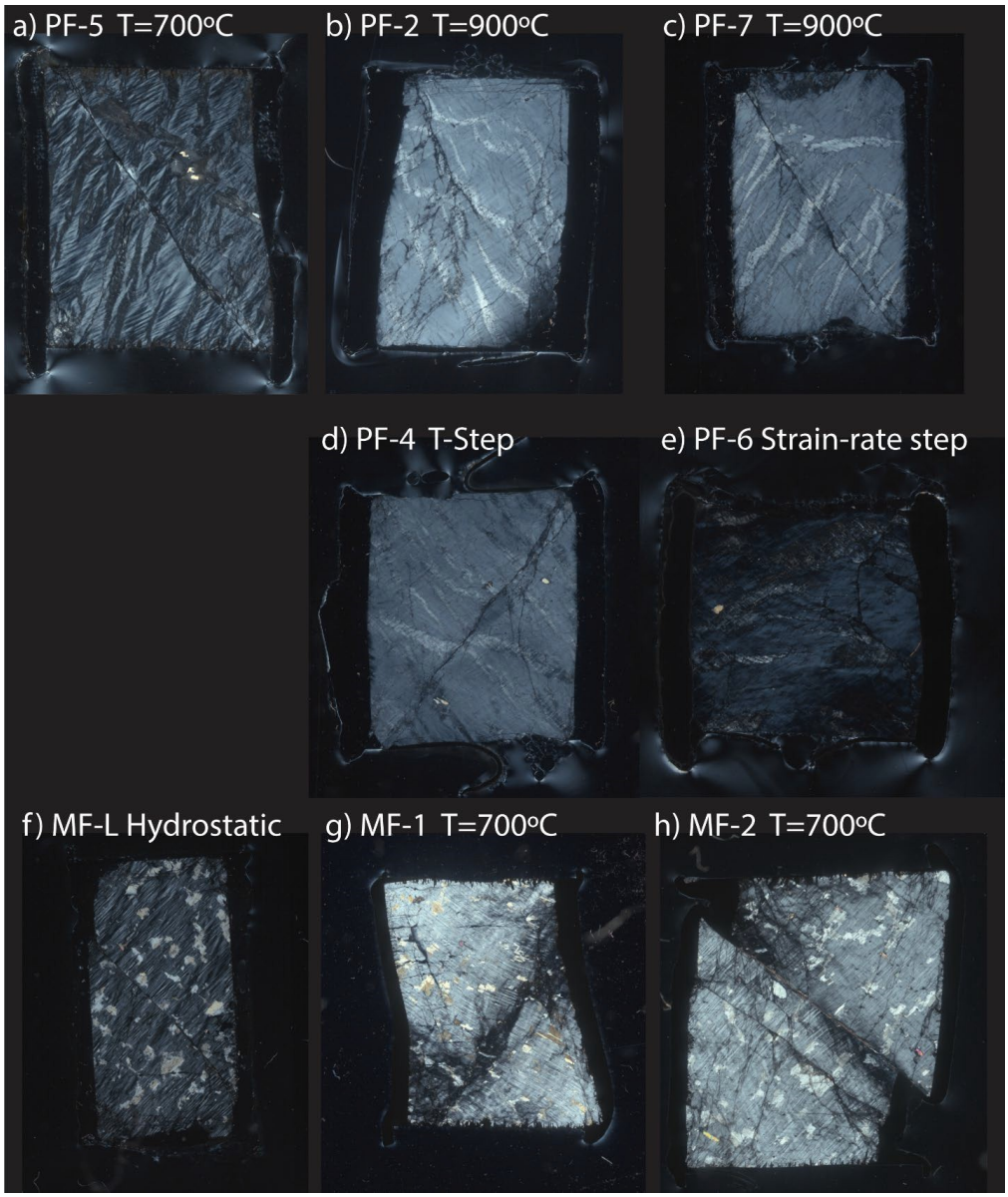

Figure 17. Full sample XPL photomicrographs are shown for deformed red perthitic microcline and white microcline samples. a) PF-5 contains albite lamellae, twins and a sample-scale fracture with 204um of offset. b) PF-2 sample contains albite lamellae, fractures propagating from the corner of the sample. Original tartan twins of the starting material are absent. c) PF-7 annealed for a week at T=800ºC at room pressure before deformation. The sample contains albite lamellae, a sample-scale fracture with 387 um of displacement. Tartan twins are absent. d) PF-4 contains a sample-scale fracture with a displacement of 550um and albite lamellae. e) PF-6 is heavily deformed and visibly barreled. f) MF-L was pressurized to Pc=1500MPa at T=300ºC and contains a sample-scale fracture with displacement of 442 um. g) MF-1 shows localized undulatory extinction along a sample-scale fracture with twins and albite inclusions throughout. h) MF-2 contains twins and undulatory extinction localized near a large sample-scale fracture with 1050um of displacement. Albite inclusions are present (light gray) throughout the sample.

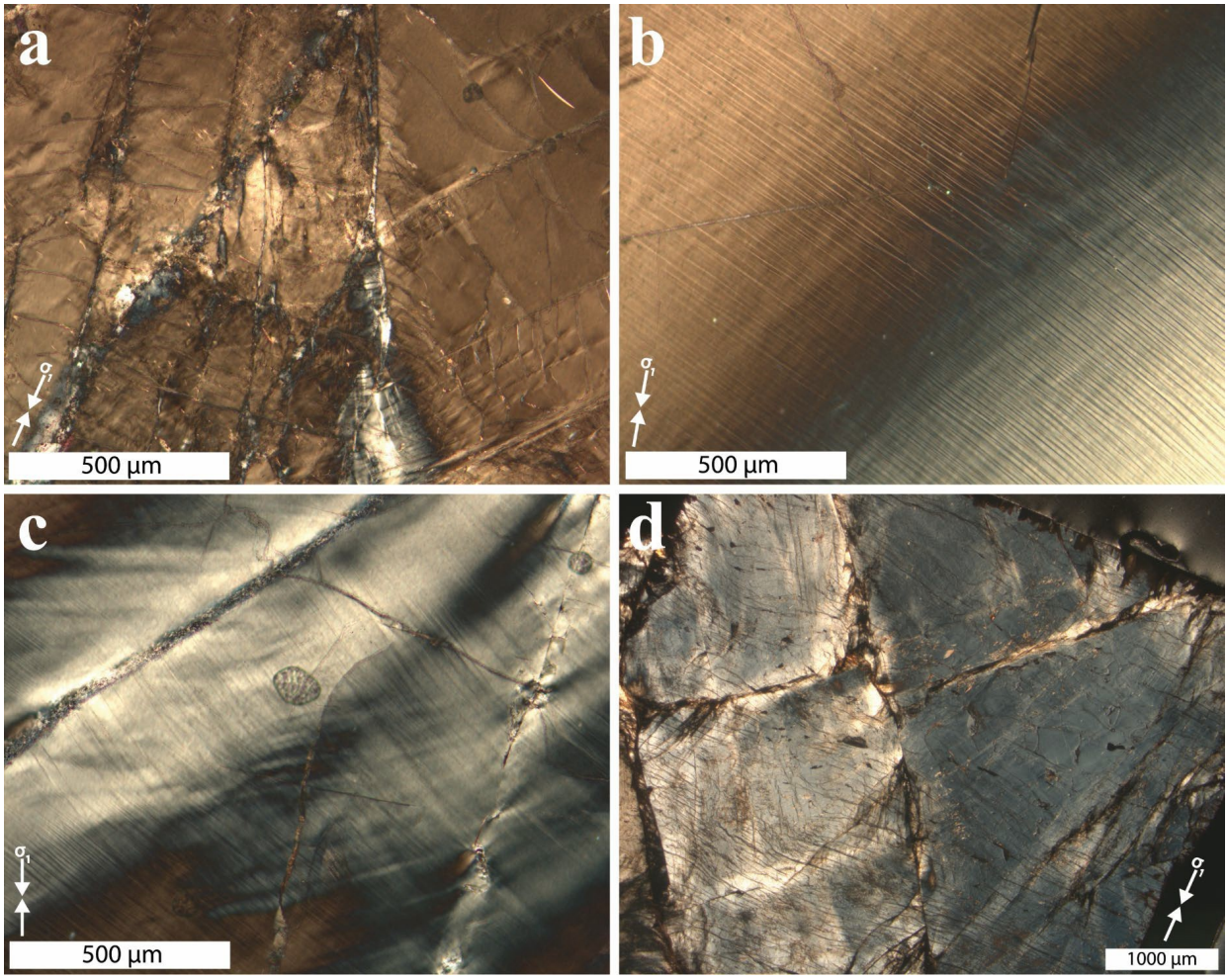

Figure 18. XPL microstructures of sanidine single crystals compressed in the [001] direction (axial load and shortening direction shown by arrows on individual photomicrographs). a) SF-1 exhibiting undulatory extinction localized near large fractures. b) SF-2 containing smooth undulatory extinction across sample and fine bands of undulatory extinction with orientations that vary due to external rotation resulting from slip. Deformation lamellae are on the (12-1) slip plane. c) SF-2 containing kink bands and undulatory extinction localized near fractures. Recrystallization is observed along the fracture plane. d) SF-1: Large, crosscutting fractures, undulatory extinction, and extension cracks perpendicular the sample axis, localized twins and kink bands near fracture planes.

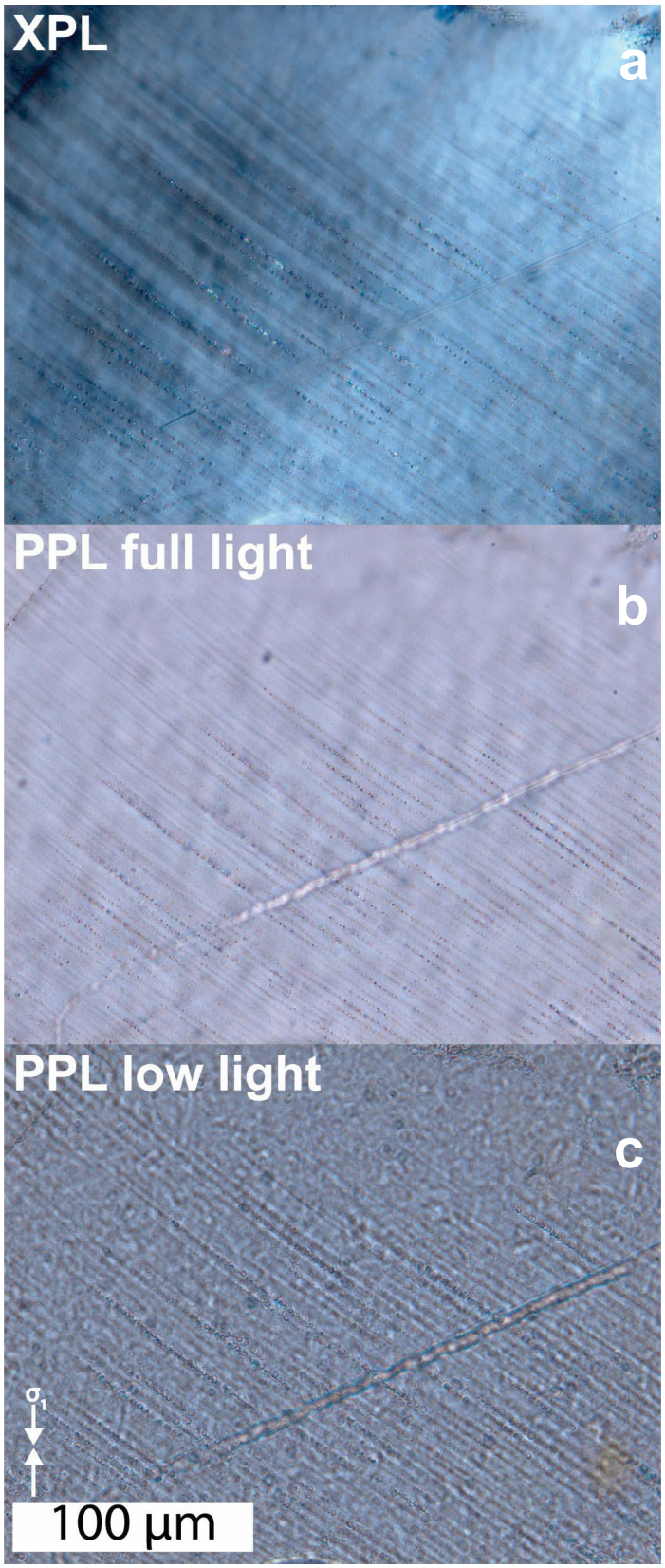

Figure 19. Photomicrographs of SF-2 in the same location under differing illumination. The images all show deformation lamellae along (12-1) with small (1 um) fluid inclusions decorating the deformation lamellae. a) Deformation lamellae lined in XPL with birefringent fluid inclusions correspond with patchy undulatory extinction. b) Deformation lamellae and fluid inclusions are visible in PPL in full light. c) Deformation lamellae in PPL accentuated by dialing down the condenser aperture to increase optical relief.

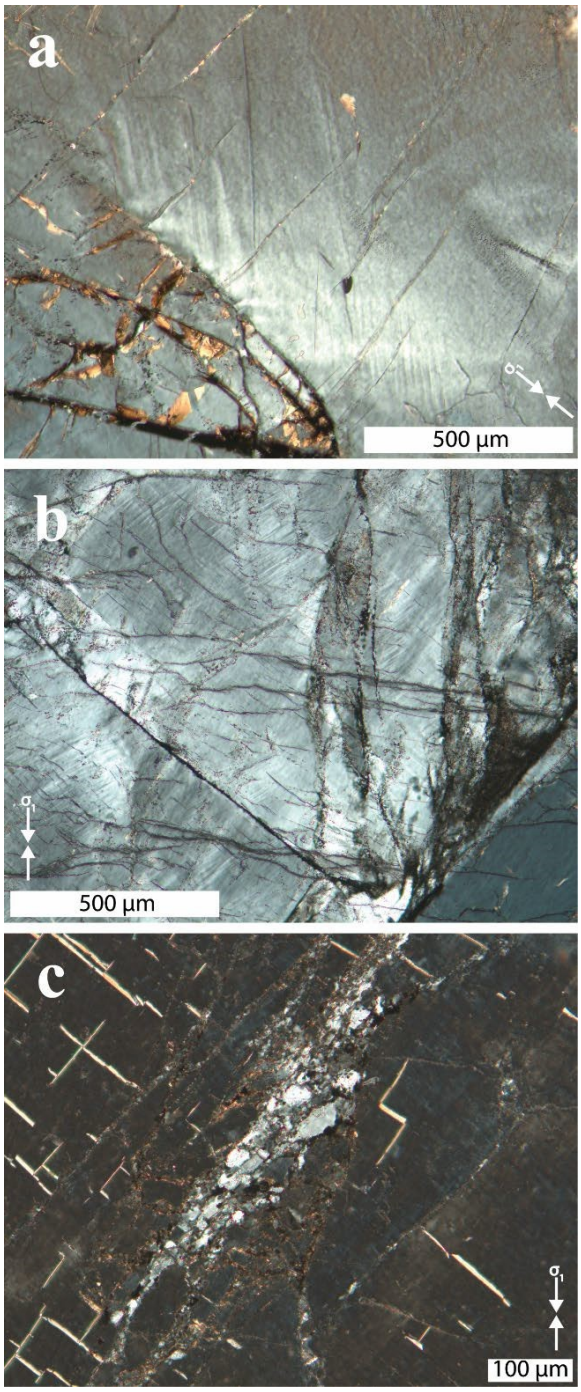

Figure 20. XPL microstructures of deformed Baveno and Adularia samples. Axial load and shortening direction shown with arrows. a) BF-2 exhibiting undulatory extinction and twins near a large fracture. b) AF-1 exhibiting undulatory extinction, twins, recrystallized grains and planes of fluid inclusions near a large fracture. c) AF-2 with newly recrystallized grains formed along large fracture. Secondary minerals occur within the starting material, sealing feldspar cleavage cracks.

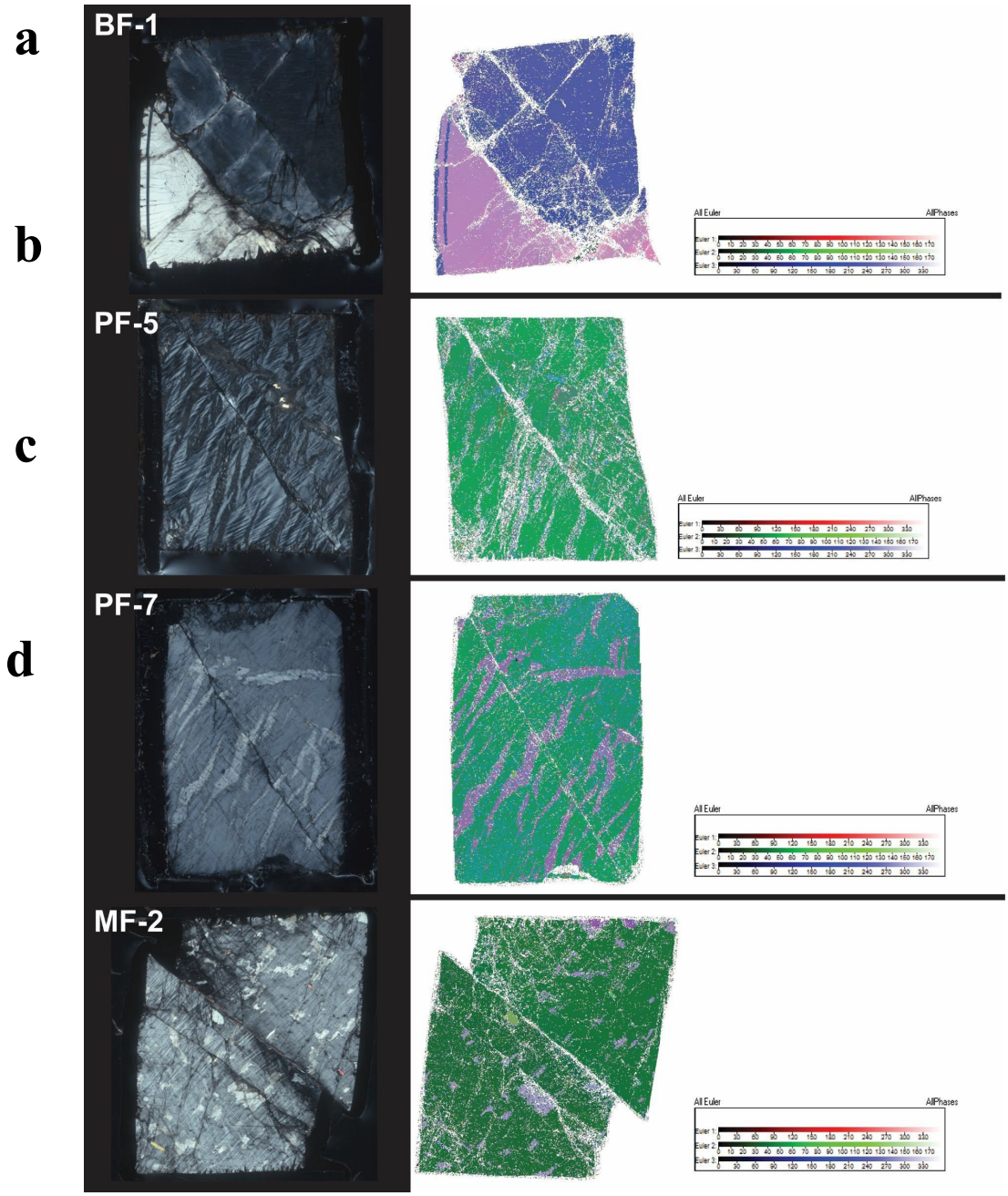

Figure 21. XPL full sample images (left) and EBSD scans (right) exhibit brittle and plastic microstructures. EBSD maps contoursed as Euler angle differences in orientation (Euler color scales on right). a) BF-1 is a bicrystal shown in XPL by differences in birefringence. The corresponding EBSD map confirms the misorientation. b) PF-5 (T=700ºC) exhibits a consistent microcline orientation (green in the EBSD map) and slightly misoriented albite lamellae. c) The EBSD map of PF-7 (annealed) shows the differences in orientation from bulk microcline (green) and albite lamellae (purple). d) MF-2 sample contours large-offset mica-lined fractures and albite lamellae.

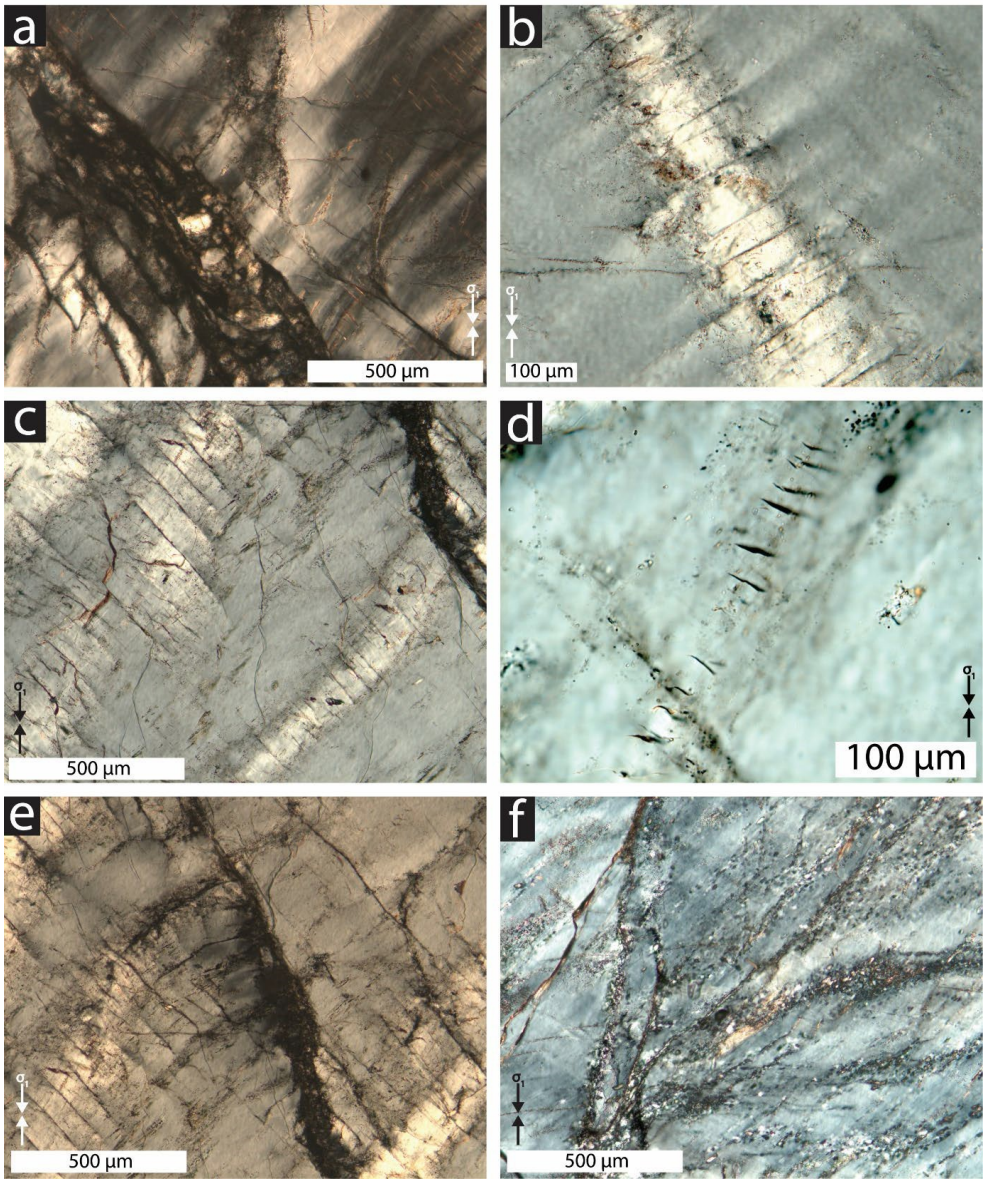

Figure *22.* XPL microstructures of deformed perthitic microcline samples (axial load and shortening direction shown vertically). a) PF-5 showing complex fracture, crushed zones and broad undulatory extinction that replaced tartan twinning throughout the low temperature (700^{o}C) PF samples. b) PF-2 exhibiting brittle cleavage cracks within albite lamellae with corresponding undulatory extinction due to slip in the surrounding microcline. c) PF-7 albite lamellae with displacement along cleavage cracks. d) PF-7 with relict cleavage fractures typical of albite lamellae in this deformed sample, but lacking albite. e) PF-7 with undulatory extinction near a major fracture, recrystallized grains and planes of fluid inclusions near fracture. f) PF-6 with recrystallized grains along planes of fluid inclusions and fractures.

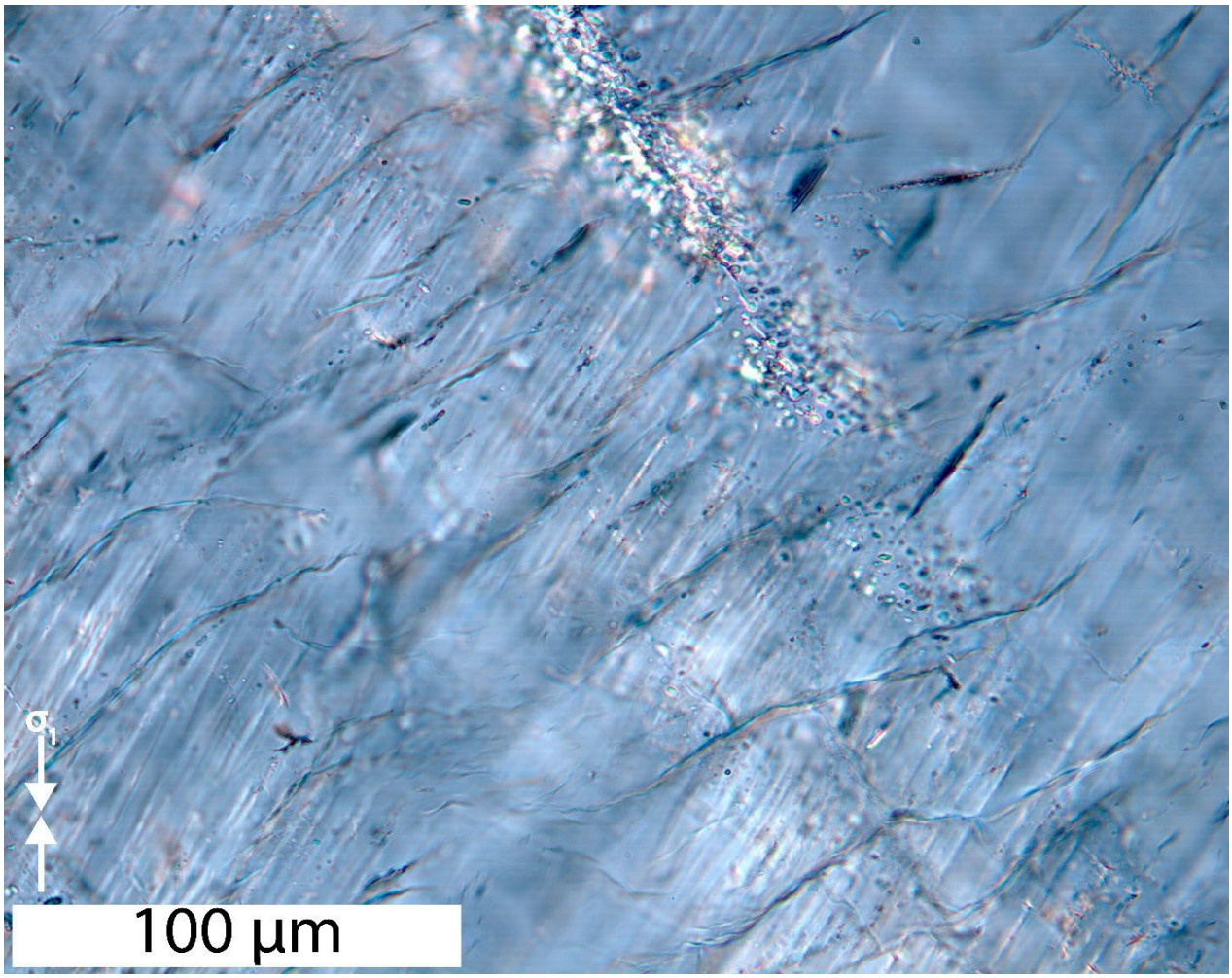

Figure *23*. XPL photomicrograph of PF-4. Showing thin parallel deformation lamellae localized within the albite exsolution lamellae, crosscut by parallel, widely spaced cleavage microcracks. The region within localized deformation and microfractures is contained within a single albite exsolution lamellae surrounded by fluid inclusions along the lamellae boundary.

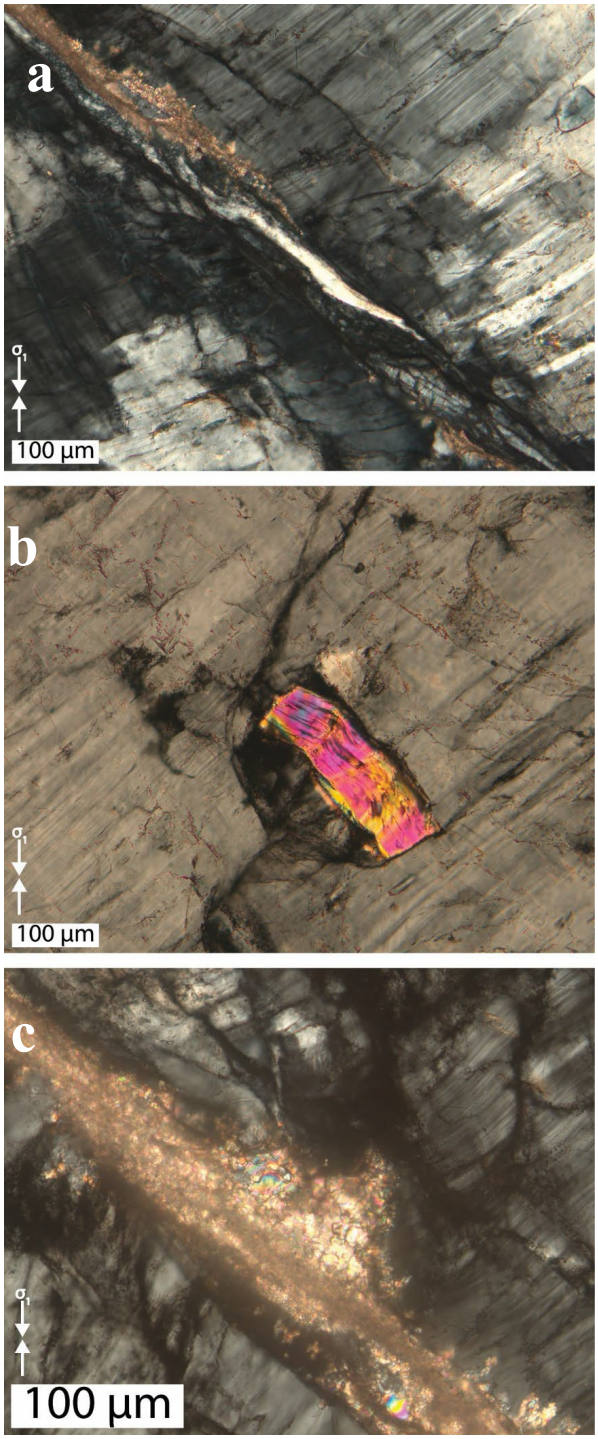

Figure *24*. Microstructures of deformed white microcline sample MF-2 (axial load and shortening direction shown vertically). a) Twins, kink bands, undulatory extinction, and recrystallization near fracture with S-C fabric development. b) Kinked muscovite inclusion within deformed white microcline feldspar single crystal. c) Fine grains of muscovite and feldspar make up gouge of large displacement (1050 um) fracture.

APPENDIX B TABLES

Feldspar	Deformation Mechanism	Temp.	Confining Pressure (MPa)	Strain Rate	References	H (kJ/mol)	n	Stress Strain
Synthetic anorthite and anorthite-diopside polycrystals	Diffusion creep	1100-1300°C	0.1	Creep tests	Dimanov et al., 1999; Dimanov et al., 2003	377-585	1.0	
Synthetic anorthite polycrystals	Diffusion creep	1000-1300°C	0.1	Creep tests	Wang et al., 1996	240	2.5	
Plagioclase single crystals (An60)	'soft' orientation: dislocation slip on (010) [001],(001) ½ <110>, less common slip on {111} ½ <110>, (131) [101],(242) [101] 'Hard' orientation: brittle and plastic deformation	900°C	1000	7.5-8.7 x 10^{-7} s^{-1}	Stünitz et al., 2003			Hard orientation, H2O added steady state = ~800°C. Hard orientation steady state =~500°C. Soft orientation steady state ~300MPa
Plagioclase single crystals (An1 - An77)	Brittle fracture, albite and pericline twinning, dislocation slip on (010) [100], (010) ½[201], (001) [100], (101) ½ [111], (101) ½ [111], (101) [101], (112) ½ [201], (132) ½ [201], (132) ½ [111]	800°C	1000	$2x10^{-5}$ s^{-1}	Borg and Heard, 1970; Marshall and McLaren, 1977			Yield stress (kbar): (880°C, Pc=10kbar, 2.2-10.7 kbar); (800°C, Pc= 8kbar, 1.9-7.0 kbar); (500°C, Pc=5kbar, 6-6.5kbar)
Sanidine single crystals	Dislocation glide at 700 °C, dislocation glide and climb at 900 °C, slip on (010) [100], (010) [001], (001) ½ [110], (110) ½ [112],(111) ½ [110],(121) [101]	700-1100°C	1600	$2x10^{-6}$ s^{-1}	Willaime et al., 1979; Kovacs and Gandais, 1980; Scandale et al., 1983			
Polycrystalline Hale albite	Both brittle and plastic deformation mechanisms	600-900°C	1500	$3x10^{-6}$ s^{-1}	Tullis and Yund, 1980			

Synthetic fine-grained anorthite aggregates					Rybacki and Dresen, 2000	356-648 or 170-467	3.0 or 1.0	

Table 1. Previous studies of feldspar slip systems summarized for different varieties of feldspar experimental conditions and listed for previous experimental studies of feldspar deformation. Best-fit H* and n values and mechanical results

Table 2. Compositions, Trace Water Contents and Type of Water of Feldspar Single Crystals Used in This Study

Feldspar		Water Type	Water Content (ppm)	Chemical Formula
Sanidine P1	SFP1	OH on K sites	18*	$(K_{0.97}Na_{0.04}Fe_{0.04})Al_{0.97}Si_{2.99}O_8$
Sanidine P2	SFP2	OH on K sites	17*	$(K_{0.96}Na_{0.04}Fe_{0.06})Al_{0.94}Si_{3.00}O_8$
Baveno	BF	OH defects	4950*	$(K_{0.82}Na_{0.162}Ca_{0.003}Ba_{0.005}Fe_{0.001})Al_{1.046}Si_{2.964}O_8$
Adularia	AF	H2O on K sites	615*	$(K_{0.87}Na_{0.09}Ba_{0.04})Al_{1.07}Si_{2.94}O_8$
White Microcline	MF	H2O inclusions	2210**	$(K_{0.94}Na_{0.07})Al_{1.03}Si_{2.98}O_8$
White Albite	MF			$(K_{0.01}Na_{0.97}Ca_{0.02})Al_{1.03}Si_{2.98}O_8$
Red Microcline	PF	H2O inclusions	2380**	$(K_{0.96}Na_{0.04})Al_{1.01}Si_{2.99}O_8$
Red Albite	PF			$(K_{0.01}Na_{0.97}Ca_{0.01})Al_{1.02}Si_{2.99}O_8$

*in molar ppm H_2O per formula unit feldspar $(K,Na)AlSi_3O_8$ based on absorbance calibrations of Mosenfeldre et al. (2015) **in molar ppm of H_2O in fluid inclusions per formular unit feldspar based on calibration of Shannon Castro (Texas A&M University, personal communication)

83

Table 3. List of Experiments on Potassium Feldspar Single Crystals.

Material	Exp.	Temp. (^oC)	$\dot{\varepsilon}$ (s^{-1})	Yield		Peak		3% strain post-yield		Final		Hardening Coefficient,h (MPa)
				Stress (MPa)	Strain (%)	Stress (MPa)	Strain (%)	Stress (MPa)	Strain (%)	Stress (MPa)	Strain (%)	
Sanidine	SF-1	700	1.6×10^{-6}	613	2.5	718	3.4	685	5.5	522	16.9	-
Sanidine	SF-2*	900	1.8×10^{-6}	135	1.9	240	18.9	195	4.9	240	19.5	218.6
Baveno	BF-1	700	1.8×10^{-6}	584	2.8	707	6.2	267	5.4	687	17.3	-
Baveno	BF- 2	900	1.6×10^{-6}	140	2.5	-	-	275	5.0	209 326	19.1	225.9
Adularia	AF- 1	700	1.7×10^{-6}	204	2.4	32	18.9	705	5.8	261	19.6	847.6;
Adularia	AF- 2	900		227	2.0		3.7	177		452	20.5	141.5**
Red Perthite	PF-5	700	1.6×10^{-6}	550	2.5	6			5.5		16.9	-
			1.7×10^{-6}				3.4	560				-
						281	3.5	181	5.5			
						608						
Red Perthite	PF-2	900	1.6×10^{-6}	173	2.5	184			5.5	175	20.6	-
Red Perthite	PF-7	900	2.0×10^{-6}	184	1.8	-	-	215	4.8	262	19.2	388.7
White Microcline	MF-1	700	1.7×10^{-6}	544	3.0	701	5.6	700	6.0	517	19.0	-
		700								259	17.3	-
White Microcline	MF-2		1.8×10^{-6}	483	3.6	556	5.3	529	6.6			
Red Perthite	PF-6	900	1.6×10^{-6}	132	1.5	-	-	175	4.5	177	4.9	470.0
			6.7×10^{-6}	160	1.7	-	-	206	4.7	216	7.9	370.0
			1.9×10^{-5}	182	2.1	-	-	240	51	245	6.6	534.4
			7.9×10^{-5}	218	2.6	308	10.9	292	5.6	307	11.1	313.4
			2.1×10^{-4}	248	3.2	-	-	325	6.2	376	13.1	784.8
			2.7×10^{-6}	42	1.3	-	-	86	4.3	104	11.4	198.8
Red Perthite	PF-4	950	1.7×10^{-6}	139	1.9	-	-	176	4.9	178	5.5	786.4
		900	1.7×10^{-6}	160	1.7	-	-	196	4.7	198	5.1	381.9

	800	**1.6×10^{-6}**	**228**	**1.6**	**294**	**5.5**	**293**	**4.6**	**292**	**5.9**	**311.2**
	700	**1.6×10^{-6}**	**318**	**1.6**	**-**	**-**	**434**	**4.6**	**447**	**7.6**	**557.6**
	650	**1.6×10^{-6}**	**398**	**1.6**	**-**	**-**	**557**	**4.6**	**616**	**9.1**	**1426.4**

Note: All experiments were conducted at Pc = 1500 MPa in a Griggs solid-medium piston-cylinder apparatus. * SF-2 compressed in the [001] direction. All other samples were deformed in the [012] direction. **847.6 MPa= h for 5-10% strain; 141.5 MPa = h for 10-20% strain